International Journal of Applied Mechanics
Vol. 1, No. 1 (2009) 137–177

Imperial College Press
www.icpress.co.uk

SIMULATING THE FLUID DYNAMICS OF NATURAL AND PROSTHETIC HEART VALVES USING THE IMMERSED BOUNDARY METHOD

BOYCE E. GRIFFITH

Leon H. Charney Division of Cardiology
New York University School of Medicine
550 First Avenue, New York, New York 10016, USA
boyce.griffith@nyumc.org

XIAOYU LUO

Department of Mathematics
University of Glasgow
University Gardens, Glasgow G12 8QW, UK
x.y.luo@maths.gla.ac.uk

DAVID M. McQUEEN* and CHARLES S. PESKIN†

Courant Institute of Mathematical Sciences
New York University, 251 Mercer Street
New York, New York 10012, USA
**mcqueen@cims.nyu.edu*
†peskin@cims.nyu.edu

Received 12 February 2009
Accepted 25 February 2009

The immersed boundary method is both a general mathematical framework and a particular numerical approach to problems of fluid-structure interaction. In the present work, we describe the application of the immersed boundary method to the simulation of the fluid dynamics of heart valves, including a model of a natural aortic valve and a model of a chorded prosthetic mitral valve. Each valve is mounted in a semi-rigid flow chamber. In the case of the mitral valve, the flow chamber is a circular pipe, and in the case of the aortic valve, the flow chamber is a model of the aortic root. The model valves and flow chambers are immersed in a viscous incompressible fluid, and realistic fluid boundary conditions are prescribed at the upstream and downstream ends of the chambers. To connect the immersed boundary models to the boundaries of the fluid domain, we introduce a novel modification of the standard immersed boundary scheme. In particular, near the outer boundaries of the fluid domain, we modify the construction of the regularized delta function which mediates fluid-structure coupling in the immersed boundary method, whereas in the interior of the fluid domain, we employ a standard four-point delta function which is frequently used with the immersed boundary method. The standard delta function is used wherever possible, and the modified delta function continuously transitions to the standard delta function away from the outer boundaries of the fluid domain. Three-dimensional computational results are presented to demonstrate the capabilities of our immersed boundary approach to simulating the fluid dynamics of heart valves.

Keywords: Immersed boundary method; fluid-structure interaction; physical boundary conditions; aortic valve; mitral valve; prosthetic valve; adaptive mesh refinement.

1. Introduction

The immersed boundary method [Peskin, 2002] is a general mathematical framework for problems in which a rigid or elastic structure is immersed in a fluid flow, and it is also a numerical approach to simulating such problems. A particular example is the dynamic interaction of a flexible heart valve leaflet and the blood in which it is immersed. Indeed, the immersed boundary method was introduced to model and to simulate such problems [Peskin, 1972, 1977]. In this work, we present the application of a recent version of the immersed boundary method [Griffith and Peskin, 2005; Griffith *et al.*, 2007, 2009] to the simulation of heart valve dynamics in three spatial dimensions.

For problems of fluid-structure interaction, the immersed boundary method couples an Eulerian description of the fluid to a Lagrangian description of the immersed structure. In the continuous setting, interaction between fluid and structure variables is mediated by integral transforms with Dirac delta function kernels. When the continuous immersed boundary formulation is discretized for computer simulation, the Dirac delta function kernels are replaced by regularized versions of the delta function. This approach allows the fluid variables to be treated using efficient Cartesian grid methods while allowing for a fully Lagrangian treatment of the immersed structure. Moreover, the immersed boundary approach does not require the generation of body conforming meshes. Consequently, the immersed boundary method is well-suited for problems in which the structure undergoes significant movement or is subject to large deformations.

In this paper, we present two different immersed boundary simulations of heart valves, including a simulation of a natural aortic valve (the valve which prevents backflow from the aorta into the left ventricle of the heart), and a simulation of a chorded prosthetic mitral valve (the valve which prevents regurgitation from the left ventricle of the heart into the left atrium of the heart). In our simulations, each valve is mounted in a semi-rigid flow chamber which is immersed in a viscous incompressible fluid. For the mitral valve simulation, the flow chamber is a circular pipe, and for the aortic valve simulation, the flow chamber is a model of an idealized human aortic root (the base of the aorta, which attaches to the heart). In each case, the flow chamber is constructed as an immersed boundary model which attaches to the outer boundaries of the fluid domain. At these domain boundaries, fluid boundary conditions provide upstream (driving) and downstream (loading) conditions for the flow chambers. In most previous work using the immersed boundary method, the computational domain was assumed to be periodic (i.e., periodic boundary conditions were employed for the fluid), or the immersed elastic structure was not allowed to approach closely to the outer boundary of the fluid domain or to attach to the outer boundary of the fluid domain. To enable the attachment of immersed structures to domain boundaries where physical boundary conditions are employed, we introduce in this paper a novel extension of the immersed boundary method. This extension involves modifying the regularized delta function which mediates

Lagrangian-Eulerian interaction; however, this modification is required only within a narrow region near the boundaries of the fluid domain. In the remainder of the computational domain, we are able to employ a standard four-point regularized delta function which is frequently used with the immersed boundary method.

2. The Immersed Boundary Method

2.1. *Mathematical formulation*

In the immersed boundary approach to fluid-structure interaction, the viscous incompressible fluid is described using the Eulerian incompressible Navier-Stokes equations, and a Lagrangian formulation is used to describe the elasticity of the immersed elastic structure. In the present work, we assume that the fluid possesses a uniform mass density ρ and dynamic viscosity μ, and that the immersed elastic structure is neutrally buoyant.[a] Let $\mathbf{x} = (x, y, z) \in U$ denote Cartesian (physical) coordinates, where U is the physical domain, let $(q, r, s) \in \Omega$ denote Lagrangian (material) coordinates attached to the structure, where Ω is the Lagrangian coordinate domain, and let $\mathbf{X}(q, r, s, t) \in U$ denote the physical position of material point (q, r, s) at time t. Throughout the present work, U is assumed to be a rectangular box, so that $U = [0, \ell_{\mathrm{x}}] \times [0, \ell_{\mathrm{y}}] \times [0, \ell_{\mathrm{z}}]$. The equations of motion for the coupled fluid-structure system are

$$\rho \left(\frac{\partial \mathbf{u}}{\partial t} + (\mathbf{u} \cdot \nabla)\mathbf{u} \right) + \nabla p = \mu \nabla^2 \mathbf{u} + \mathbf{f}, \tag{2.1}$$

$$\nabla \cdot \mathbf{u} = 0, \tag{2.2}$$

$$\mathbf{f}(\mathbf{x}, t) = \int_{\Omega} \mathbf{F}(q, r, s, t)\, \delta(\mathbf{x} - \mathbf{X}(q, r, s, t))\, \mathrm{d}q\, \mathrm{d}r\, \mathrm{d}s, \tag{2.3}$$

$$\frac{\partial \mathbf{X}}{\partial t}(q, r, s, t) = \int_{U} \mathbf{u}(\mathbf{x}, t)\, \delta(\mathbf{x} - \mathbf{X}(q, r, s, t))\, \mathrm{d}\mathbf{x}, \tag{2.4}$$

$$\mathbf{F}(\cdot, \cdot, \cdot, t) = \boldsymbol{\mathcal{F}}[\mathbf{X}(\cdot, \cdot, \cdot, t)]. \tag{2.5}$$

Equations (2.1) and (2.2) are the incompressible Navier-Stokes equations, which are written in terms of the fluid velocity $\mathbf{u}(\mathbf{x}, t) = (u(\mathbf{x}, t), v(\mathbf{x}, t), w(\mathbf{x}, t))$ and pressure $p(\mathbf{x}, t)$, along with a body force $\mathbf{f}(\mathbf{x}, t)$ which is the Eulerian elastic force density (i.e., the elastic force density with respect to the Cartesian coordinates $\mathbf{x} = (x, y, z)$) applied by the structure to the fluid. Eq. (2.5) indicates that the Lagrangian elastic force density (i.e., the elastic force density with respect to the curvilinear

[a] The immersed boundary method is not restricted to problems in which the structure is neutrally buoyant in the fluid. Indeed, several versions of the immersed boundary method have been developed to treat the case in which the mass density of the immersed structure is *different* from that of the fluid [Peskin, 2002; Zhu and Peskin, 2002, 2003; Kim, 2003; Kim *et al.*, 2003; Kim and Peskin, 2006, 2007]. Additionally, work underway at the Courant Institute and elsewhere aims to develop a version of the method which treats the case in which the viscosity of the structure is different from that of the fluid.

coordinates (q, r, s)) generated by the elasticity of the structure is determined by a time-independent mapping of the configuration of the immersed structure.[b] The particular Lagrangian force mapping $\boldsymbol{\mathcal{F}}$ employed in the present work is described in Sec. 3.

Next, we turn our attention to the two Lagrangian-Eulerian interaction equations, Eqs. (2.3) and (2.4). Both equations employ integral transformations which use the three-dimensional Dirac delta function $\delta(\mathbf{x}) = \delta(x)\,\delta(y)\,\delta(z)$ to convert between Lagrangian and Eulerian quantities. Eq. (2.4) states that the structure moves at the local fluid velocity, i.e.,

$$\frac{\partial \mathbf{X}}{\partial t}(q, r, s, t) = \mathbf{u}(\mathbf{X}(q, r, s, t), t), \tag{2.6}$$

which is the no-slip condition of a viscous fluid. The delta-function formulation in Eq. (2.4) is equivalent to Eq. (2.6) but has the advantage that it can be discretized to obtain an interpolation formula; see Eq. (2.13), below. In this context, the no-slip condition is used to determine the motion of the immersed elastic structure rather than to constrain the motion of the fluid. Note that the no-slip condition will also appear below as a physical boundary condition on the tangential fluid velocity along the boundary of the physical domain U.

The remaining interaction equation, Eq. (2.3), converts the Lagrangian elastic force density $\mathbf{F}$ into the equivalent Eulerian elastic force density $\mathbf{f}$. It is important to note that generally $\mathbf{F}(q, r, s, t) \neq \mathbf{f}(\mathbf{X}(q, r, s, t), t)$; however, $\mathbf{F}$ and $\mathbf{f}$ are nonetheless equivalent *as densities*. This can be seen as follows. Let $V \subseteq U$ be an arbitrary region in U, and let $\mathbf{X}^{-1}(V, t) = \{(q, r, s) : \mathbf{X}(q, r, s, t) \in V\}$ denote the set of all material points of the immersed structure which are physically located in region V at time t. We verify that $\mathbf{F}$ and $\mathbf{f}$ are equivalent densities by computing

$$\int_V \mathbf{f}(\mathbf{x}, t)\,\mathrm{d}\mathbf{x} = \int_V \left(\int_\Omega \mathbf{F}(q, r, s, t)\,\delta(\mathbf{x} - \mathbf{X}(q, r, s, t))\,\mathrm{d}q\,\mathrm{d}r\,\mathrm{d}s \right) \mathrm{d}\mathbf{x} \tag{2.7}$$

$$= \int_\Omega \left(\int_V \mathbf{F}(q, r, s, t)\,\delta(\mathbf{x} - \mathbf{X}(q, r, s, t))\,\mathrm{d}\mathbf{x} \right) \mathrm{d}q\,\mathrm{d}r\,\mathrm{d}s \tag{2.8}$$

$$= \int_{\mathbf{X}^{-1}(V,t)} \mathbf{F}(q, r, s, t)\,\mathrm{d}q\,\mathrm{d}r\,\mathrm{d}s. \tag{2.9}$$

Thus, the total force applied to the region V at time t is equal to the total force generated by the material points of the structure which are physically located in the region V at time t.

Along the boundary of the physical domain U, we impose no-slip boundary conditions on the tangential components of the fluid velocity, along with either Dirichlet boundary conditions on the normal component of the velocity or prescribed normal traction boundary conditions. Note that here, the no-slip condition is in fact a

[b]Heart valves are essentially passive structures, and their elastic properties may be considered to be time independent. To simulate an *active* elastic material, such as contracting and relaxing cardiac muscle tissue, $\boldsymbol{\mathcal{F}}$ would need to be a time-dependent mapping of the structure configuration.

constraint on the fluid motion, whereas in Eq. (2.6), the no-slip condition does not constrain the fluid motion but instead determines the motion of the immersed structure. Since the fluid is incompressible and Newtonian, the combination of no-slip tangential velocity boundary conditions and normal traction boundary conditions is equivalent to a prescribed-pressure boundary condition. This may be seen as follows: Let $\mathbf{n} = \mathbf{n}(\mathbf{x}_{\mathrm{b}})$ denote the outward unit normal at a position $\mathbf{x}_{\mathrm{b}}$ along the domain boundary ∂U, and let $\boldsymbol{\tau} = \boldsymbol{\tau}(\mathbf{x}_{\mathrm{b}})$ denote the unit tangent vector at $\mathbf{x}_{\mathrm{b}} \in \partial U$. The stress tensor for a viscous incompressible fluid is

$$\boldsymbol{\sigma} = -p\mathbb{I} + \mu \left[\nabla \mathbf{u} + (\nabla \mathbf{u})^T \right]. \tag{2.10}$$

Prescribing the normal traction at the boundary is equivalent to prescribing the normal component of the normal stress,

$$\mathbf{n} \cdot \boldsymbol{\sigma} \cdot \mathbf{n} = -p + 2\mu \frac{\partial}{\partial n}(\mathbf{u} \cdot \mathbf{n}), \tag{2.11}$$

at the boundary. Since we impose no-slip tangential velocity boundary conditions, $\mathbf{u} \cdot \boldsymbol{\tau} \equiv 0$ along the domain boundary, and the incompressibility constraint therefore implies that $\frac{\partial}{\partial n}(\mathbf{u} \cdot \mathbf{n}) \equiv 0$ along the boundary. Thus, in this case, the normal component of the normal stress is simply $\mathbf{n} \cdot \boldsymbol{\sigma} \cdot \mathbf{n} = -p$. To make this clearer, recall that $U = [0, \ell_{\mathrm{x}}] \times [0, \ell_{\mathrm{y}}] \times [0, \ell_{\mathrm{z}}]$, and consider the boundary $x = \ell_{\mathrm{x}}$. Along this boundary, $\mathbf{n} = (1, 0, 0)$ is the outward unit normal, and the normal component of the normal stress is $-p + 2\mu \frac{\partial u}{\partial x}$. The no-slip conditions imposed on the tangential components of the fluid velocity imply that $v \equiv 0$ and $w \equiv 0$ along the $x = \ell_{\mathrm{x}}$ boundary, and thus $\frac{\partial v}{\partial y} = \frac{\partial w}{\partial z} = 0$ along that boundary as well. The incompressibility constraint therefore implies that $\frac{\partial u}{\partial x} = 0$ along the $x = \ell_{\mathrm{x}}$ boundary, so that the normal component of the normal traction at that boundary is simply $-p$. Similar computations demonstrate that $\mathbf{n} \cdot \boldsymbol{\sigma} \cdot \mathbf{n} = -p$ along the other boundaries of the physical domain U. For additional details on physical boundary conditions for the incompressible Navier-Stokes equations, including a discussion of alternative choices of physical boundary conditions, see Ch. 3 Sec. 8 of Gresho and Sani [1998].

In our simulation of the aortic valve, we use prescribed-pressure boundary conditions to connect the detailed immersed boundary models to reduced models of the left ventricle of the heart (at the upstream boundary) and the systemic arterial tree (at the downstream boundary). For our simulation of the mitral valve, we prescribe an upstream driving velocity and use zero-pressure boundary conditions at the outflow boundary. Physical boundary conditions are also imposed on the fluid in the exterior region of U located outside of the flow chambers, and for both models, a combination of solid wall (no-slip and no-penetration) boundary conditions and zero-pressure boundary conditions is imposed along these exterior domain boundaries. Each immersed boundary model attaches to two faces of U, and solid wall boundary conditions are used along the exterior portion of each face to which the model attaches, thereby anchoring the immersed boundary model to ∂U. Zero-pressure boundary conditions are used along the remainder of the exterior

fluid domain boundary, i.e., along the four faces to which no immersed boundary model is attached. This allows the exterior domain to accommodate changes in the volumes of the flow chambers, which expand slightly when pressurized because they are only semi-rigid.[c] A schematic diagram showing the attachment of the aortic root model to ∂U is shown in Fig. 1; the mitral valve model is similar.

To determine appropriate initial conditions, we assume that the fluid is initially at rest, so that $\mathbf{u} \equiv 0$, and that there is no applied normal traction along the boundary at the initial time $t = t^0$. Although the pressure p is not a state variable for an incompressible fluid and does not require an initial condition, in the case that the structure is initialized in an unstressed configuration, it follows that $p \equiv 0$ at time $t = t^0$. Otherwise, the initial pressure may be determined by the forces applied by the structure to the fluid at the initial time.

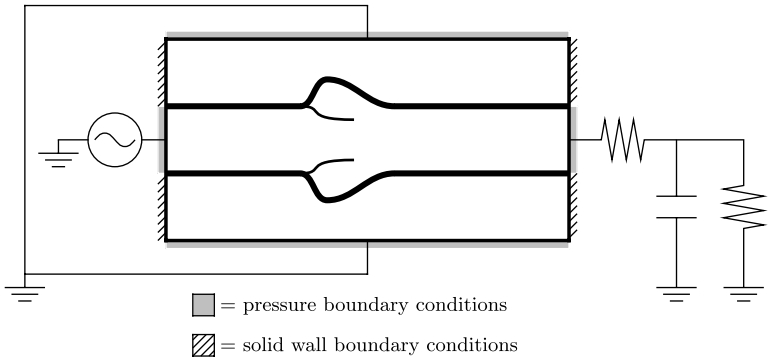

Fig. 1. Two-dimensional schematic diagram showing the attachment of the model aortic valve and root to the outer boundary ∂U of the rectangular fluid domain U, along with the reduced models which provide driving and loading conditions. (Note that the fluid-structure interaction models and computations of the present work are actually three-dimensional.) At each position along the outer boundary of the fluid domain, either pressure boundary conditions or solid wall boundary conditions are imposed on the fluid. Pressure boundary conditions are employed at the ends of the model vessel to connect the model aortic root to a prescribed, time-dependent pressure source at its upstream boundary, and to a reduced ordinary differential equation model of the systemic arterial tree at its downstream boundary. Solid wall boundary conditions are imposed along a portion of the domain boundary to which the model vessel is attached in order to anchor the vessel to ∂U. Zero-pressure boundary conditions are used along the remainder of ∂U, allowing the exterior fluid to accommodate changes in the volume of the flow chamber, which expands slightly when pressurized since it is only semi-rigid. The mitral valve model is similar, except that a time-dependent velocity profile is prescribed at the upstream boundary of the model flow chamber, and zero-pressure boundary conditions are imposed at the downstream boundary.

[c]For incompressible flows, the pressure is uniquely defined only up to an additive constant. If the pressure were to be shifted by a constant c (i.e., if we were to redefine the pressure as $p'(\mathbf{x}, t) = p(\mathbf{x}, t) + c$), the same shift c must be applied to *all* of the reference pressures which are used to determine the pressure boundary conditions. In particular, redefining the pressure as $p' = p + c$ and shifting each of the reference pressures used to determine the pressure boundary conditions by the same value c yields the same dynamics, independent of the choice of c.

2.2. *Spatial discretization*

In the numerical treatment of the continuous immersed boundary equations of motion, the Eulerian variables are discretized on a Cartesian grid and the Lagrangian variables are discretized on a curvilinear mesh which moves with the structure. In the present work, we employ a uniform Cartesian grid for our simulation of the mitral valve and an adaptively refined Cartesian grid for our simulation of the aortic valve. For simplicity, we present our numerical scheme only in the uniform grid setting. See Griffith *et al.* [2007, 2009] for further details on the use of adaptive mesh refinement in the context of the immersed boundary method.

To simplify the exposition, we assume for the remainder of Sec. 2 that the computational domain U is the unit cube, i.e., that $\ell_{\mathrm{x}} = \ell_{\mathrm{y}} = \ell_{\mathrm{z}} = 1$. In the uniform grid case, U is discretized on a regular $N \times N \times N$ Cartesian grid with grid spacings $\Delta x = \Delta y = \Delta z = h = \frac{1}{N}$. (The generalization to the case of a rectangular box is straightforward.) The fluid variables, including the three components of the velocity and the pressure, are defined at the centers of the cells of the Cartesian grid. Let (i, j, k) label the individual Cartesian grid cells for integer values of i, j, and k, $0 \leq i, j, k < N$, and let $\mathbf{x}_{i,j,k} = \left(\left(i + \frac{1}{2}\right) h, \left(j + \frac{1}{2}\right) h, \left(k + \frac{1}{2}\right) h\right)$ denote the physical location of the center of cell (i, j, k). Similarly, let (q, r, s) label an individual curvilinear mesh node, and let the curvilinear mesh spacings be denoted by Δq, Δr, and Δs.

The discretizations of the Lagrangian-Eulerian interaction equations, Eqs. (2.3) and (2.4), both employ the same regularized version of the Dirac delta function, denoted δ_h. The construction of δ_h is discussed below in Sec. 2.3. Let $\mathbf{X}_{q,r,s}$ denote the position of curvilinear mesh node (q, r, s), and let $\mathbf{F}_{q,r,s}$ denote the discretization of the Lagrangian elastic force density evaluated at curvilinear mesh node (q, r, s). The discretization of Eq. (2.3) is

$$\mathbf{f}_{i,j,k} = \sum_{q,r,s} \mathbf{F}_{q,r,s}\, \delta_h\left(\mathbf{x}_{i,j,k}, \mathbf{X}_{q,r,s}\right)\, \Delta q\, \Delta r\, \Delta s, \tag{2.12}$$

where $\mathbf{f}_{i,j,k}$ denotes the discretization of the Eulerian elastic force density at the centers of the Cartesian grid cells. Similarly, Eq. (2.4) is discretized as

$$\frac{\mathrm{d}}{\mathrm{d}t}\mathbf{X}_{q,r,s} = \sum_{i,j,k} \mathbf{u}_{i,j,k}\, \delta_h\left(\mathbf{x}_{i,j,k}, \mathbf{X}_{q,r,s}\right)\, \Delta x\, \Delta y\, \Delta z, \tag{2.13}$$

where $\mathbf{u}_{i,j,k}$ denotes the discretization of the Eulerian fluid velocity at the centers of the Cartesian grid cells. Note that $\delta_h(\mathbf{x}, \mathbf{X})$ is a regularized version of the singular function $\delta(\mathbf{x} - \mathbf{X})$. It is possible to view $\delta(\mathbf{x} - \mathbf{X})$ either as a function of the two variables $\mathbf{x}$ and $\mathbf{X}$, or as a function of the single variable $\mathbf{d} = \mathbf{x} - \mathbf{X}$. In the present work, however, it is necessary to make δ_h an explicit function both of the position $\mathbf{x}_{i,j,k}$ of grid cell (i, j, k) and of the position $\mathbf{X}_{q,r,s}$ of Lagrangian node (q, r, s) because *different* functions of $\mathbf{x}$, not related merely by a translation, must be used, depending on whether the Lagrangian point $\mathbf{X}_{q,r,s}$ is "close" to or "far" from the boundary ∂U of the physical domain U. In earlier versions of the immersed

boundary method, periodic boundary conditions were employed, and in that case, δ_h can be chosen as a function of $\mathbf{x}_{i,j,k} - \mathbf{X}_{q,r,s}$ alone, i.e., $\delta_h(\mathbf{x}, \mathbf{X})$ remains invariant under any translation that is applied to both variables. As we demonstrate below, if we wish to use the standard immersed boundary delta function in the interior of the domain, this simpler approach is not suitable for problems involving physical boundary conditions in which the curvilinear mesh is allowed to attach to ∂U, nor is it suitable for problems involving physical boundary conditions in which the elastic structure is allowed to approach closely ∂U.

Despite the lack of translation invariance in our construction of $\delta_h(\mathbf{x}, \mathbf{X})$, note that the *same* regularized delta function is used for a particular Lagrangian point (q, r, s) both to *interpolate* the fluid velocity from the Cartesian grid to Lagrangian point (q, r, s) and to *spread* the Lagrangian elastic force density from Lagrangian point (q, r, s) to the Cartesian grid; see Eqs. (2.12) and (2.13). This ensures that power is conserved during Lagrangian-Eulerian interaction [Peskin, 2002]. The construction of δ_h described below also ensures that force and torque are conserved.

2.3. *Construction of the regularized delta function*

In the present work, the three-dimensional regularized delta function is constructed as the tensor product of one-dimensional regularized delta functions, i.e.,

$$\delta_h(\mathbf{x}, \mathbf{X}) = \delta_h(x, X)\, \delta_h(y, Y)\, \delta_h(z, Z). \tag{2.14}$$

It is important to emphasize that in this work, the regularized delta function is an explicit function both of $\mathbf{x} = (x, y, z)$ and of $\mathbf{X} = (X, Y, Z)$ and, in particular, is *not* a function of $\mathbf{d} = \mathbf{x} - \mathbf{X}$ alone. Each one-dimensional regularized delta function is of the form

$$\delta_h(x, X) = \begin{cases} \dfrac{1}{h}\, \tilde{\phi}\left(\dfrac{x}{h}, \dfrac{X}{h}\right), & \text{if } X < \dfrac{3}{2}h, \\ \dfrac{1}{h}\, \phi\left(\dfrac{x - X}{h}\right), & \text{if } \dfrac{3}{2}h \le X \le 1 - \dfrac{3}{2}h, \quad \text{and} \\ \dfrac{1}{h}\, \tilde{\phi}\left(\dfrac{1 - x}{h}, \dfrac{1 - X}{h}\right), & \text{if } 1 - \dfrac{3}{2}h < X, \end{cases} \tag{2.15}$$

where the functions ϕ and $\tilde{\phi}$ are specified below. The function ϕ is intended to be used with Lagrangian points located in the interior of the domain, and the construction of ϕ does not account for the presence of domain boundaries. In fact, we demonstrate below that we *cannot* use ϕ to define $\delta_h(x, X)$ when X is sufficiently close to the domain boundary. On the other hand, $\tilde{\phi}$ is specifically constructed to be used in the vicinity of domain boundaries and to transition continuously to ϕ away from the boundaries of the physical domain. The location where we transition from using ϕ to using $\tilde{\phi}$ is chosen to ensure that ϕ is used wherever possible.

To construct $\delta_h(x, X)$, we first specify $\phi(r)$, which is used to define the regularized delta function away from domain boundaries where physical boundary conditions are prescribed. Following Peskin [2002], we require $\phi(r)$ to satisfy:

$$\phi(r) \text{ is a continuous function of } r, \tag{2.16}$$

$$\phi(r) = 0 \text{ for } |r| \geq 2, \tag{2.17}$$

$$\sum_{i \text{ even}} \phi(r-i) = \sum_{i \text{ odd}} \phi(r-i) = \frac{1}{2} \text{ for all real } r, \tag{2.18}$$

$$\sum_i (r-i)\phi(r-i) = 0 \text{ for all real } r, \text{ and} \tag{2.19}$$

$$\sum_i \left(\phi(r-i)\right)^2 = C \text{ for all real } r. \tag{2.20}$$

Briefly, these properties state that the regularized delta function has compact support, satisfies two discrete moment conditions, and satisfies a condition which approximates grid independence. The discrete moment conditions, Eqs. (2.18) and (2.19), imply that force and torque are conserved when forces are spread to the Cartesian grid from the curvilinear mesh, and that the interpolation operator generated by δ_h is second order accurate when interpolating smooth functions [Peskin, 2002]. It can be shown [Peskin, 2002] that the unique function which satisfies (2.16)–(2.20) is

$$\phi(r) = \begin{cases} \frac{1}{8}(3 - 2|r| + \sqrt{1 + 4|r| - 4r^2}), & 0 \leq |r| < 1, \\ \frac{1}{8}(5 - 2|r| - \sqrt{-7 + 12|r| - 4r^2}), & 1 \leq |r| < 2, \\ 0, & 2 \leq |r|\,. \end{cases} \tag{2.21}$$

For this four-point delta function, $C = \frac{3}{8}$.

The standard regularized delta function may be used with Lagrangian points located in the interior of the domain (i.e., with points which are *away* from domain boundaries). For Lagrangian points which are sufficiently close to the boundary of the physical domain, however, an alternate construction is required. To see why this is so, consider a cell-centered discretization of the half-infinite interval $[0, \infty)$. We take the grid spacing to be $h = 1$, so that the cell centers are located at the points $a_i = \left(i + \frac{1}{2}\right)$, $i = 0, 1, 2, \ldots$. Let $A \geq 0$ be a fixed value which is not constrained to be aligned with the underlying grid, and let $\phi_i = \phi(a_i - A) = \phi(i + \frac{1}{2} - A)$ denote the evaluation of $\phi(a - A)$ at cell center a_i. Note that for $A \geq \frac{3}{2}$, the construction of ϕ implies that the delta function weights ϕ_i satisfy

$$\sum_{\substack{i \geq 0 \\ i \text{ even}}} \phi_i = \sum_{\substack{i \geq 0 \\ i \text{ odd}}} \phi_i = \frac{1}{2}, \tag{2.22}$$

$$\sum_{i \geq 0} (a_i - A)\, \phi_i = \sum_{i \geq 0} \left(i + \frac{1}{2} - A\right) \phi_i = 0, \tag{2.23}$$

$$\sum_{i \geq 0} (\phi_i)^2 = C = \frac{3}{8}. \tag{2.24}$$

For $A < \frac{3}{2}$, however, *none* of these conditions is satisfied, since the sums are restricted to Cartesian cell centers that are located within the computational domain.

We wish to construct an alternative four-point delta function $\tilde{\phi}(a, A)$ for $A < \frac{3}{2}$ which (1) satisfies the discrete moment conditions, Eqs. (2.22) and (2.23); (2) satisfies the sum-of-squares condition, Eq. (2.24), wherever possible; and (3) continuously transitions to $\phi(a - A)$ as $A \to \frac{3}{2}$. In order to achieve this, we generalize the restriction on the support of ϕ as given by Eq. (2.17), so that, when A is within $\frac{3}{2}$ meshwidths of the $a = 0$ boundary, the support of $\tilde{\phi}$ is no longer restricted to two meshwidths on either side of A, but instead includes the four cell centers that are closest to the boundary. It will also turn out that we must abandon the sum-of-squares condition when A is sufficiently close to the $a = 0$ boundary; see below. Although we shall construct $\tilde{\phi}(a, A)$ only for $A < \frac{3}{2}$, note that this is sufficient to define $\delta_h(x, X)$ for all $X \in [0, 1]$; see Eq. (2.15).

Consider again a cell-centered discretization of the half-infinite interval $[0, \infty)$ with grid spacing $h = 1$. Let $0 \leq A < \frac{3}{2}$ be a fixed value, and let $\tilde{\phi}_i = \tilde{\phi}(a_i, A) = \tilde{\phi}(i + \frac{1}{2}, A)$ denote the evaluation of $\tilde{\phi}(a, A)$ at cell center a_i. We wish to determine formulae for $\tilde{\phi}_0$, $\tilde{\phi}_1$, $\tilde{\phi}_2$, and $\tilde{\phi}_3$, the modified delta function weights near the $a = 0$ boundary. In this case, the analogue of Eq. (2.22) is

$$\tilde{\phi}_0 + \tilde{\phi}_2 = \tilde{\phi}_1 + \tilde{\phi}_3 = \frac{1}{2}, \tag{2.25}$$

i.e.,

$$\tilde{\phi}_0 = \frac{1}{2} - \tilde{\phi}_2 \quad \text{and} \quad \tilde{\phi}_1 = \frac{1}{2} - \tilde{\phi}_3. \tag{2.26}$$

Similarly, the analogue of Eq. (2.23) is

$$\left(\frac{1}{2} - A\right) \tilde{\phi}_0 + \left(\frac{3}{2} - A\right) \tilde{\phi}_1 + \left(\frac{5}{2} - A\right) \tilde{\phi}_2 + \left(\frac{7}{2} - A\right) \tilde{\phi}_3 = 0. \tag{2.27}$$

Using (2.26), we have that

$$\tilde{\phi}_0 = 1 - \frac{A}{2} + \tilde{\phi}_3, \tag{2.28}$$

$$\tilde{\phi}_1 = \frac{1}{2} - \tilde{\phi}_3, \tag{2.29}$$

$$\tilde{\phi}_2 = -\frac{1}{2} + \frac{A}{2} - \tilde{\phi}_3. \tag{2.30}$$

Finally, the analogue of Eq. (2.24) is

$$(\tilde{\phi}_0)^2 + (\tilde{\phi}_1)^2 + (\tilde{\phi}_2)^2 + (\tilde{\phi}_3)^2 = \frac{3}{8}, \tag{2.31}$$

which may be expressed entirely in terms of the unknown function $\tilde{\phi}_3$ by making use of Eqs. (2.28)–(2.30). The solutions to this quadratic equation for $\tilde{\phi}_3$ are

$$\frac{A-1}{4} \pm \frac{1}{8}\sqrt{-14+16A-4A^2}. \tag{2.32}$$

Note, however, that $-14+16A-4A^2 \geq 0$ only for $A \in \left[2-\frac{\sqrt{2}}{2}, 2+\frac{\sqrt{2}}{2}\right]$. For $A > 2+\frac{\sqrt{2}}{2} > \frac{3}{2}$, we do not need to use this alternative delta function, but to avoid a complex-valued solution for $A < 2-\frac{\sqrt{2}}{2} < \frac{3}{2}$, we set

$$\tilde{\phi}_3 = \begin{cases} \dfrac{A-1}{4}, & \text{for } A < 2-\frac{\sqrt{2}}{2}, \\ \dfrac{A-1}{4} - \dfrac{1}{8}\sqrt{-14+16A-4A^2}, & \text{otherwise.} \end{cases} \tag{2.33}$$

The choice of sign ensures that $\tilde{\phi}_i = \phi_i$ for $A = \frac{3}{2}$. Moreover, by construction, $\tilde{\phi}(a, A)$ continuously approaches $\phi(a - A)$ as $A \to \frac{3}{2}$.

Note that for $A < 2-\frac{\sqrt{2}}{2}$, $\tilde{\phi}_3 = \frac{A-1}{4}$, and the modified delta function weights are simply

$$\tilde{\phi}_0 = \frac{3-A}{4} \tag{2.34}$$

$$\tilde{\phi}_1 = \frac{3-A}{4} \tag{2.35}$$

$$\tilde{\phi}_2 = \frac{A-1}{4} \tag{2.36}$$

$$\tilde{\phi}_3 = \frac{A-1}{4}. \tag{2.37}$$

It is interesting to note that for $A < 2-\frac{\sqrt{2}}{2}$, these delta function weights are "optimal" in that of all possible four-point delta function weights which satisfy the discrete moment conditions at the $a = 0$ boundary (i.e., Eqs. (2.26) and (2.27)), these weights have minimum Euclidean norm and, moreover, come the closest to satisfying the sum-of-squares condition. To see that this is so, suppose that w_0, w_1, w_2, and w_3 are alternative weights which satisfy only the two discrete moment conditions, i.e., that w_0, w_1, w_2, and w_3 are defined by

$$w_0 = 1 - \frac{A}{2} + \omega, \tag{2.38}$$

$$w_1 = \frac{1}{2} - \omega, \tag{2.39}$$

$$w_2 = -\frac{1}{2} + \frac{A}{2} - \omega, \tag{2.40}$$

$$w_3 = \omega, \tag{2.41}$$

where $\omega = \omega(A)$ is as yet undetermined. Let E denote the sum of the squares of these weights, i.e.,

$$E = (w_0)^2 + (w_1)^2 + (w_2)^2 + (w_3)^2 \tag{2.42}$$

$$= \left(1 - \frac{A}{2} + \omega\right)^2 + \left(\frac{1}{2} - \omega\right)^2 + \left(-\frac{1}{2} + \frac{A}{2} - \omega\right)^2 + (\omega)^2. \tag{2.43}$$

It is straightforward to verify that

$$\frac{\partial E}{\partial \omega} = 2 - 2A + 8\omega, \quad \text{and} \tag{2.44}$$

$$\frac{\partial^2 E}{\partial \omega^2} = 8, \tag{2.45}$$

so that $\frac{\partial E}{\partial \omega} = 0$ and $\frac{\partial^2 E}{\partial \omega^2} > 0$ for $\omega = \frac{A-1}{4}$, and thus E is minimized when $w_i = \tilde{\phi}_i$. Moreover, for $A < 2 - \frac{\sqrt{2}}{2}$ and $\omega = \frac{A-1}{4}$, $E > \frac{3}{8} = C$. Since E is minimized when $\omega = \frac{A-1}{4}$, it therefore follows that $|E - C|$ is also minimized when $w_i = \tilde{\phi}_i$.

This completes our discussion of the construction of $\delta_h(\mathbf{x}, \mathbf{X})$. Note that in the foregoing, we have determined $\delta_h(\mathbf{x}, \mathbf{X})$ for all $\mathbf{X} \in U$, but we have not determined $\delta_h(\mathbf{x}, \mathbf{X})$ for all $\mathbf{x} \in U$. Instead, we have considered only the special cases in which $\mathbf{x}$ is the center of a Cartesian grid cell located within U. In practice, these are the only cases that are needed; see Eqs. (2.12) and (2.13). Finally, although we have explicitly treated only the cell-centered case corresponding to the four-point delta function, similar formulae may be obtained for alternate Eulerian discretizations (e.g., node-centered or staggered-grid discretizations) and for alternate delta functions (e.g., the six-point delta function introduced in Stockie [1997], or the three-point delta function used in Roma *et al.* [1999]).

2.4. *Cartesian grid finite difference and projection operators*

To solve the incompressible Navier-Stokes equations in the uniform grid case, we employ standard second-order accurate, cell-centered approximations to the gradient, divergence, and Laplace operators, as well as a cell-centered approximate projection operator defined below. In the adaptive case, it is necessary to develop approximations to the gradient, divergence, and Laplace operators for locally refined Cartesian grids, along with a locally refined approximate projection operator, and in the present work, we employ cell-centered approximations on such grids which are essentially the same as those of Martin and Colella [2000]; Martin *et al.* [2008]. In either the uniform or locally-refined case, for a scalar function ψ, we denote by $(\mathbf{G}\psi)_{i,j,k}$ the approximation to $\nabla\psi$ evaluated at cell center $\mathbf{x}_{i,j,k}$. Similarly, for a vector field $\mathbf{u}$, the approximation to $\nabla\cdot\mathbf{u}$ evaluated at $\mathbf{x}_{i,j,k}$ is denoted by $(\mathbf{D}\cdot\mathbf{u})_{i,j,k}$. Finally, the evaluation of the approximation to $\nabla^2\psi$ at $\mathbf{x}_{i,j,k}$ is denoted by $(L\psi)_{i,j,k}$. It is important to note that $\mathbf{D}\cdot\mathbf{G} \neq L$. See Griffith and Peskin [2005]; Griffith *et al.* [2007] for further details.

To motivate the approximate projection operator we use to enforce the incompressibility constraint on the velocity field to second order accuracy, we first state a discrete version of the Hodge decomposition, the theorem which forms the basis of projection methods for incompressible flow problems [Chorin, 1968, 1969; Bell *et al.*, 1989]. Given a cell-centered vector field $\mathbf{w} = \mathbf{w}_{i,j,k}$, $\mathbf{w}$ may be decomposed as

$$\mathbf{w} = \mathbf{v} + \mathbf{G}\varphi, \tag{2.46}$$

where $\mathbf{D} \cdot \mathbf{v} = 0$. Moreover, this decomposition is unique, i.e., the vector fields $\mathbf{v}$ and $\mathbf{G}\varphi$ are uniquely determined by Eq. (2.46) together with the condition $\mathbf{D} \cdot \mathbf{v} = 0$ and suitable physical boundary conditions. This is true despite the non-uniqueness of φ, to which one may add any mesh function in the nullspace of $\mathbf{G}$ without changing $\mathbf{v}$ or $\mathbf{G}\varphi$. The discrete Hodge decomposition, Eq. (2.46), leads to the definition of the operator P which constructs $\mathbf{v}$ from $\mathbf{w}$ via

$$\mathbf{v} = P\mathbf{w} = \mathbf{w} - \mathbf{G}\varphi = (I - \mathbf{G}\left(\mathbf{D} \cdot \mathbf{G}\right)^{-1}\mathbf{D} \cdot)\mathbf{w}. \tag{2.47}$$

For any vector field $\mathbf{w}$, $\mathbf{D} \cdot P\mathbf{w} = 0$, so that $P^2\mathbf{w} = P\mathbf{w}$. Thus, P is a projection operator. The operator P is referred to as an *exact* projection operator, since $\mathbf{v} = P\mathbf{w}$ exactly satisfies the divergence-free condition $\left(\mathbf{D} \cdot \mathbf{v}\right)_{i,j,k} = 0$.[d]

In practice, the application of the exact projection operator P requires the solution of a system of linear equations of the form $\mathbf{D} \cdot \mathbf{G}\varphi = \mathbf{D} \cdot \mathbf{w}$. Developing efficient solvers for the operator $\mathbf{D} \cdot \mathbf{G}$ is difficult, however. For instance, on a uniform, periodic, three-dimensional Cartesian grid with an even number of grid cells in each coordinate direction, $\mathbf{D} \cdot \mathbf{G}$ has an eight-dimensional nullspace. Developing solvers for $\mathbf{D} \cdot \mathbf{G}$ in the case that physical boundary conditions are imposed on the physical domain U is also challenging. Moreover, the use of P in the solution of the incompressible Navier-Stokes equations leads to the well-known "checkerboard" instability. The difficulties posed by exact projections are only compounded in the presence of local mesh refinement.

In an attempt to overcome many of the difficulties associated with exact projections, many authors have replaced P by an approximation to the projection operator which only requires the development of simpler linear solvers. The first approximate projection method was described in Almgren *et al.* [1996], and in the present work, we employ an approximate projection operator which, in the uniform grid case, is the same as that of Lai [1993] and, in the locally-refined case, is essentially the same as the one described by Martin and Colella [2000]; Martin *et al.* [2008]. This approximate projection operator $\tilde{P}$ is the same as P, except that the operator $\mathbf{D} \cdot \mathbf{G}$ is replaced by L, i.e.,

$$\tilde{P}\mathbf{w} = (I - \mathbf{G}\left(L\right)^{-1}\mathbf{D} \cdot)\mathbf{w}. \tag{2.48}$$

[d]The divergence-free condition is not enforced exactly by P in practice, but instead is enforced to a level determined by the accuracy of the solver for the linear system $\mathbf{D} \cdot \mathbf{G}\varphi = \mathbf{D} \cdot \mathbf{w}$, and by the floating point accuracy of the computer.

It is important to note that $\tilde{P}$ is *not* a projection operator, since $L \neq \mathbf{D} \cdot \mathbf{G}$. For smooth $\mathbf{w}$, however, $\|\mathbf{D} \cdot \tilde{P}\mathbf{w}\| \to 0$ as the Cartesian grid is refined, and in the uniform grid case, $|\mathbf{D} \cdot \tilde{P}\mathbf{w}| = \mathcal{O}(h^2)$ pointwise. Note also that P and $\tilde{P}$ are both finite difference approximations to the *continuous* operator $I - \nabla \left(\nabla^2\right)^{-1} \nabla\cdot$.

2.5. *Timestepping*

We now summarize the timestepping scheme used in the present work. Let Δt denote the uniform timestep size, so that $\Delta t = t^{n+1} - t^n$ is the duration of the n^{th} timestep. When we employ adaptive mesh refinement, all levels of the locally refined grid are advanced synchronously in time (i.e., we do not employ *subcycled* timestepping [Almgren *et al.*, 1998; Martin and Colella, 2000; Martin *et al.*, 2008]). At the beginning of each timestep $n \geq 0$, we possess approximations to the values of the state variables at time t^n, namely $\mathbf{u}^n$ and $\mathbf{X}^n$. The pressure (which is in principle not a state variable) is defined at half-timesteps to obtain a consistent second-order accurate method, and at the beginning of each timestep $n > 0$, we also possess an approximation to the pressure $p^{n-\frac{1}{2}}$ defined at the midpoint of the previous time interval. Recall that we assume that $\mathbf{u} \equiv 0$ at the initial time $t = t^0$. If necessary, a simple iterative scheme is employed during the first timestep to determine an initial value for the pressure [Griffith and Peskin, 2005].

To advance the solution forward in time from $t = t^n$ to $t = t^{n+1}$, we first compute $\mathbf{X}^{(n+1)}$, where the parentheses around $n+1$ indicate that this is only a *preliminary* approximation to the locations of the nodes of the curvilinear mesh at time t^{n+1}. This initial approximation to the updated structure configuration is obtained by approximating Eq. (2.13) by

$$\mathbf{X}^{(n+1)}_{q,r,s} = \mathbf{X}^n_{q,r,s} + \Delta t \sum_{i,j,k} \mathbf{u}^n_{i,j,k}\, \delta_h\left(\mathbf{x}_{i,j,k}, \mathbf{X}^n_{q,r,s}\right)\, \Delta x\, \Delta y\, \Delta z. \tag{2.49}$$

A discrete approximation to $\boldsymbol{\mathcal{F}}[\mathbf{X}(\cdot,\cdot,\cdot)]$ provides the curvilinear elastic force densities corresponding to the current $\mathbf{X}^n$ and updated $\mathbf{X}^{(n+1)}$ structure configurations, which are respectively denoted by $\mathbf{F}^n$ and $\mathbf{F}^{(n+1)}$. The equivalent current and updated Cartesian elastic force densities are obtained as in Eq. (2.12) and are given by

$$\mathbf{f}^n_{i,j,k} = \sum_{q,r,s} \mathbf{F}^n_{q,r,s}\, \delta_h(\mathbf{x}_{i,j,k}, \mathbf{X}^n_{q,r,s})\, \Delta q\, \Delta r\, \Delta s, \tag{2.50}$$

$$\mathbf{f}^{(n+1)}_{i,j,k} = \sum_{q,r,s} \mathbf{F}^{(n+1)}_{q,r,s}\, \delta_h(\mathbf{x}_{i,j,k}, \mathbf{X}^{(n+1)}_{q,r,s})\, \Delta q\, \Delta r\, \Delta s. \tag{2.51}$$

A timestep-centered approximation to the Cartesian elastic force density is then defined by $\mathbf{f}^{n+\frac{1}{2}} = \frac{1}{2}(\mathbf{f}^n + \mathbf{f}^{(n+1)})$.

Next, we compute the updated velocity field in two steps. First, we compute an intermediate velocity field $\mathbf{u}^*$ by solving an approximation to the momentum equation, Eq. (2.1), without imposing the constraint of incompressibility. Instead, the

time-lagged pressure gradient $\mathbf{G}p^{n-\frac{1}{2}}$ is used to approximate the pressure gradient at time $t = t^{n+\frac{1}{2}}$, so that

$$\rho\left(\frac{\mathbf{u}^* - \mathbf{u}^n}{\Delta t} + \mathbf{N}^{n+\frac{1}{2}}\right) + \mathbf{G}p^{n-\frac{1}{2}} = \frac{\mu}{2}L\left(\mathbf{u}^* + \mathbf{u}^n\right) + \mathbf{f}^{n+\frac{1}{2}}, \tag{2.52}$$

where $\mathbf{N}^{n+\frac{1}{2}} \approx [(\mathbf{u}\cdot\nabla)\mathbf{u}]^{n+\frac{1}{2}}$ is obtained via an explicit, second-order accurate Godunov method which is briefly discussed in Sec. 2.6. Second, we obtain $\mathbf{u}^{n+1}$ by approximately projecting $\mathbf{u}^*$,

$$\mathbf{u}^{n+1} = \tilde{P}\mathbf{u}^*, \tag{2.53}$$

thereby obtaining an approximation to $\mathbf{u}$ at time $t = t^{n+1}$ which satisfies the constraint of incompressibility to $\mathcal{O}(h^2)$.

Having obtained the updated velocity, we next compute the updated pressure. The value of $p^{n+\frac{1}{2}}$ is obtained by approximately projecting a *different* intermediate velocity field, denoted $\tilde{\mathbf{u}}^*$, which is obtained from a *different* treatment of the momentum equation. Unlike Eq. (2.52), this alternative treatment of the momentum equation *does not* include *any* approximation to the timestep-centered pressure gradient, so that

$$\rho\left(\frac{\tilde{\mathbf{u}}^* - \mathbf{u}^n}{\Delta t} + \mathbf{N}^{n+\frac{1}{2}}\right) = \frac{\mu}{2}L\left(\tilde{\mathbf{u}}^* + \mathbf{u}^n\right) + \mathbf{f}^{n+\frac{1}{2}}. \tag{2.54}$$

To obtain $p^{n+\frac{1}{2}}$ from $\tilde{\mathbf{u}}^*$, we first compute $\tilde{\varphi}$, the solution to a discrete Poisson problem,

$$L\tilde{\varphi} = \mathbf{D}\cdot\tilde{\mathbf{u}}^*, \tag{2.55}$$

and then obtain $p^{n+\frac{1}{2}}$ by evaluating

$$p^{n+\frac{1}{2}} = \left(I - \frac{\Delta t}{\rho}\frac{\mu}{2}L\right)\tilde{\varphi}. \tag{2.56}$$

Since we employ an approximate projection operator instead of an exact one, the values of $\tilde{P}\mathbf{u}^*$ and $\tilde{P}\tilde{\mathbf{u}}^*$ will generally be different, and therefore the approximations to the pressure obtained from the approximate projections of $\mathbf{u}^*$ and $\tilde{\mathbf{u}}^*$ are generally different. Note that $p^{n+\frac{1}{2}}$ has no influence on the value obtained for $\mathbf{u}^{n+1}$, but that it is used in the next timestep, when computing $\mathbf{u}^{n+2}$.

To complete the timestep, we obtain $\mathbf{X}^{n+1}$ by evaluating

$$\begin{aligned}\mathbf{X}_{q,r,s}^{n+1} = \mathbf{X}_{q,r,s}^{n} + \frac{\Delta t}{2}\Bigg(&\sum_{i,j,k}\mathbf{u}_{i,j,k}^{n}\,\delta_h\left(\mathbf{x}_{i,j,k}, \mathbf{X}_{q,r,s}^{n}\right)\,\Delta x\,\Delta y\,\Delta z \\ &+ \sum_{i,j,k}\mathbf{u}_{i,j,k}^{n+1}\,\delta_h\left(\mathbf{x}_{i,j,k}, \mathbf{X}_{q,r,s}^{(n+1)}\right)\,\Delta x\,\Delta y\,\Delta z\Bigg),\end{aligned} \tag{2.57}$$

which is an explicit formula for $\mathbf{X}^{n+1}$, since $\mathbf{X}^{(n+1)}$ is already defined; see Eq. (2.49).

In the foregoing scheme, note that the configuration $\mathbf{X}_{q,r,s}$ of the elastic structure is updated in Eqs. (2.49) and (2.57) via a strong stability-preserving Runge-Kutta method [Gottlieb *et al.*, 2001]. Additionally, the approximate projection method takes the form of a *hybrid* approximate projection method [Almgren *et al.*, 2000]; see Griffith and Peskin [2005]; Griffith *et al.* [2007] for further details.

2.6. *Adaptive mesh refinement and other implementation details*

In the simulation results presented in Sec. 4.2, we solve the incompressible Navier-Stokes equations on an adaptively refined hierarchical Cartesian grid like that of Fig. 2 (see also Fig. 15). The locally refined grid is constructed in a manner which ensures that the immersed structure remains covered throughout the simulation by the grid cells which comprise the finest level of the hierarchical Cartesian grid. To avoid complicating the discretization of the equations of Lagrangian-Eulerian interaction, additional Cartesian grid cells are added to the finest level of the locally refined grid to ensure that for each curvilinear mesh node (q, r, s), the support of the regularized delta function centered about $\mathbf{X}_{q,r,s}$ is also covered by the grid cells which comprise the finest level of the locally refined grid. Consequently, we are able to employ the standard discrete Lagrangian-Eulerian interaction equations (e.g., Eqs. (2.12) and (2.13)) without modification in the adaptive scheme.

The hybrid approximate projection method employed in the present work to solve the incompressible Navier-Stokes equations is largely the same as the scheme which we have used previously [Griffith and Peskin, 2005; Griffith *et al.*, 2007, 2009]. The primary differences between the scheme used in the present work and that described in Griffith and Peskin [2005]; Griffith *et al.* [2007, 2009] are summarized as follows: (1) We have found that the L-stable implicit treatment of the viscous terms in the incompressible Navier-Stokes equations used in Griffith and Peskin [2005]; Griffith *et al.* [2007, 2009] does not appear to yield any noticeable improvement in the stability of the scheme or in the quality of the numerical results when compared to the simpler Crank-Nicolson scheme. Consequently, in the present

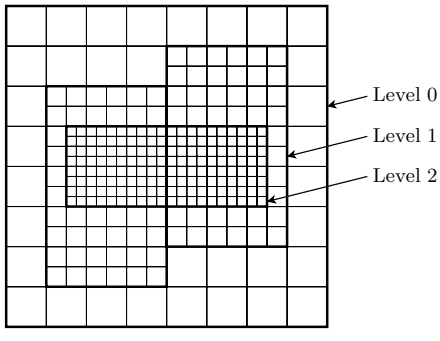

Fig. 2. An adaptively refined hierarchical Cartesian grid comprised of three nested levels.

work we employ the more computationally efficient Crank-Nicolson scheme, which is A-stable but not L-stable. (2) The explicit, second-order accurate Godunov scheme employed in the present work is essentially the same as that used in Griffith and Peskin [2005]; Griffith *et al.* [2007, 2009]; however, the Godunov method of the present work employs the xsPPM7 method of Rider *et al.* [2007] (a recent version of the piecewise parabolic method (PPM) of Colella and Woodward [1984]) to perform the initial extrapolation instead of the piecewise linear scheme of Griffith and Peskin [2005]; Griffith *et al.* [2007, 2009]. (3) Following Martin and Colella [2000]; Martin *et al.* [2008], quadratic interpolation is employed at coarse-fine interfaces to compute cell-centered values located in the ghost cells located on the "coarse side" of coarse-fine interfaces. In the method of Griffith *et al.* [2007, 2009], simpler linear interpolation was used at coarse-fine interfaces. (4) Dirichlet boundary conditions on the normal and tangential components of the fluid velocity are specified using methods introduced by Brown *et al.* [2001], and normal traction boundary conditions are specified using methods by Yang and Prosperetti [2006].

Although the methods of Brown *et al.* [2001] and of Yang and Prosperetti [2006] allow our fluid solver to treat accurately both prescribed-velocity and prescribed-traction boundary conditions, we have found that additional care is required to attach immersed boundary models to domain boundaries where physical boundary conditions are prescribed. First, we have found that it is useful to include in the model fixed Lagrangian points which are anchored to the outer domain boundary. These boundary anchor points are placed on the boundary of the domain, and they neither spread force to the Cartesian grid nor interpolate velocity from the Cartesian grid. Instead, they serve as fixed points to which other Lagrangian points may be attached (e.g., via stiff springs). In our experience, if boundary anchor points are *not* included in the model, immersed structures which are attached to the domain boundary tend to develop leaks near the boundary. Second, we have found that it is generally necessary to include an additional body force near the domain boundaries where physical boundary conditions are prescribed to penalize deviations from the prescribed-velocity boundary conditions. (No such forces appear to be required in the case of prescribed-traction boundary conditions.) Within these "fringe" or "sponge" regions [Bodony, 2006], we apply an *additional* body force to the fluid which is of the general form

$$\mathbf{f}_{i,j,k}^{\text{fringe}} = (\kappa_{i,j,k}^{\text{x}}(u_{i,j,k}^{\text{presc}} - u_{i,j,k}), \kappa_{i,j,k}^{\text{y}}(v_{i,j,k}^{\text{presc}} - v_{i,j,k}), \kappa_{i,j,k}^{\text{z}}(w_{i,j,k}^{\text{presc}} - w_{i,j,k})), \tag{2.58}$$

where $\mathbf{u}^{\text{presc}} = (u^{\text{presc}}, v^{\text{presc}}, w^{\text{presc}})$ is the prescribed velocity at the nearest domain boundary, and where $\kappa^{\text{x}}, \kappa^{\text{y}}, \kappa^{\text{z}}$ are spatially-varying feedback-forcing coefficients, which are of the form

$$\kappa_{i,j,k}^{\text{x}} = \begin{cases} \dfrac{1}{2}\dfrac{\rho}{\Delta t}, & \text{if } \mathbf{x}_{i,j,k} \text{ is located in the fringe region for } u, \\ 0, & \text{otherwise,} \end{cases} \tag{2.59}$$

$$\kappa^{\mathrm{y}}_{i,j,k} = \begin{cases} \dfrac{1}{2}\dfrac{\rho}{\Delta t}, & \text{if } \mathbf{x}_{i,j,k} \text{ is located in the fringe region for } v, \\ 0, & \text{otherwise,} \end{cases} \tag{2.60}$$

$$\kappa^{\mathrm{z}}_{i,j,k} = \begin{cases} \dfrac{1}{2}\dfrac{\rho}{\Delta t}, & \text{if } \mathbf{x}_{i,j,k} \text{ is located in the fringe region for } w, \\ 0, & \text{otherwise.} \end{cases} \tag{2.61}$$

It is important to note that the fringe region associated with a particular velocity component includes *only* those portions of U which are close to domain boundaries where Dirichlet conditions are prescribed for that velocity component. Our experience suggests that the fringe region need include only one or two layers of grid cells in the vicinity of the domain boundary.

3. Material Elasticity

We describe the properties of the model valves and flow chambers in terms of systems of elastic fibers which resist extension, compression, and bending. In the case of our model of the natural aortic valve, these fibers can be viewed as representing the collagen fibers which support the significant pressure load borne by the closed valve when the left ventricle is relaxed. In the case of the mitral valve, the fibers which comprise the leaflets are assigned material properties which approximate those of a polyurethane prosthetic mitral valve developed at the University of Glasgow. Fibers are also used to model the artificial chordae tendineae of the prosthetic mitral valve.

We shall determine the elastic force generated by deformations to the structure configuration in terms of an elastic energy functional $E = E[\mathbf{X}(\cdot,\cdot,\cdot,t)]$. The elastic force density $\mathbf{F}$ generated by deformations to the structure can be expressed in terms of the Fréchet derivative of E, i.e.,

$$\mathbf{F} = -\frac{\wp E}{\wp \mathbf{X}}, \tag{3.62}$$

which is shorthand for

$$\wp E[\mathbf{X}(\cdot,\cdot,\cdot,t)] = -\int_{\Omega} \mathbf{F}(q,r,s,t) \cdot \wp \mathbf{X}(q,r,s,t)\, \mathrm{d}q\, \mathrm{d}r\, \mathrm{d}s. \tag{3.63}$$

Note that we use the symbol $\wp$ to denote the perturbation operator instead of the traditional symbol δ because we already use δ to denote the Dirac delta function.

Suppose that the Lagrangian coordinates (q,r,s) have been chosen so that each fixed value of (q,r) labels a particular fiber. Thus, for a fixed value of the pair $(q,r) = (q_0,r_0)$, the mapping $s \to \mathbf{X}(q_0,r_0,s)$ is a parametric representation of the fiber labeled by (q_0,r_0). (Note that s is not assumed to be arc length, and even if s is chosen to be arc length in the initial or reference configuration of the structure, it will generally not remain arc length as the structure deforms.) We decompose the

elastic energy functional E into a stretching energy E_{s} and a bending energy E_{b}. The stretching energy is of the form

$$E_{\mathrm{s}} = \int_{\Omega} \mathcal{E}_{\mathrm{s}} \left(\left| \frac{\partial \mathbf{X}}{\partial s} \right| ; q, r, s \right) \, \mathrm{d}q \, \mathrm{d}r \, \mathrm{d}s, \tag{3.64}$$

where $\mathcal{E}_{\mathrm{s}}$ is the local stretching energy. Following Peskin [2002], we apply the perturbation operator to both sides of Eq. (3.64) and obtain

$$\wp E_{\mathrm{s}}[\mathbf{X}(\cdot,\cdot,\cdot,t)] = -\int_{\Omega} \frac{\partial}{\partial s} \left(\mathcal{E}_{\mathrm{s}}' \left(\left| \frac{\partial \mathbf{X}}{\partial s} \right| ; q, r, s \right) \frac{\partial \mathbf{X}/\partial s}{|\partial \mathbf{X}/\partial s|} \right) \cdot \wp \mathbf{X} \, \mathrm{d}q \, \mathrm{d}r \, \mathrm{d}s, \tag{3.65}$$

where $\mathcal{E}_{\mathrm{s}}'$ is the derivative of $\mathcal{E}_{\mathrm{s}}$ with respect to its first argument. The extension- and compression-resistant force $\mathbf{F}_{\mathrm{s}}$ is thus

$$\mathbf{F}_{\mathrm{s}} = \frac{\partial}{\partial s} \left(\mathcal{E}_{\mathrm{s}}' \left(\left| \frac{\partial \mathbf{X}}{\partial s} \right| ; q, r, s \right) \frac{\partial \mathbf{X}/\partial s}{|\partial \mathbf{X}/\partial s|} \right). \tag{3.66}$$

Letting $\boldsymbol{\tau} = \partial \mathbf{X}/\partial s / |\partial \mathbf{X}/\partial s|$ denote the unit tangent vector aligned with the fiber direction, and letting $T = \mathcal{E}_{\mathrm{s}}' \left(|\partial \mathbf{X}/\partial s| ; q, r, s \right)$ denote the fiber tension, this is

$$\mathbf{F}_{\mathrm{s}} = \frac{\partial}{\partial s} \left(T \boldsymbol{\tau} \right). \tag{3.67}$$

The bending energy is taken to be of the form

$$E_{\mathrm{b}} = \frac{1}{2} \int_{\Omega} c_{\mathrm{b}}(q, r, s) \left| \frac{\partial^2 \mathbf{X}}{\partial s^2} - \frac{\partial^2 \mathbf{X}^0}{\partial s^2} \right|^2 \mathrm{d}q \, \mathrm{d}r \, \mathrm{d}s, \tag{3.68}$$

where $c_{\mathrm{b}} = c_{\mathrm{b}}(q, r, s)$ is the bending stiffness, and where $\mathbf{X}^0 = \mathbf{X}^0(\cdot,\cdot,\cdot)$ is the reference configuration, which in the present work is generally taken to be the initial structure configuration, i.e., $\mathbf{X}^0(q, r, s) = \mathbf{X}(q, r, s, t^0)$. Applying the perturbation operator to both sides of Eq. (3.68), we find that

$$\wp E_{\mathrm{b}}[\mathbf{X}(\cdot,\cdot,\cdot,t)] = \int_{\Omega} c_{\mathrm{b}}(q, r, s) \left(\frac{\partial^2 \mathbf{X}}{\partial s^2} - \frac{\partial^2 \mathbf{X}^0}{\partial s^2} \right) \cdot \frac{\partial^2}{\partial s^2} \wp \mathbf{X} \, \mathrm{d}q \, \mathrm{d}r \, \mathrm{d}s. \tag{3.69}$$

Integrating by parts twice, we find that

$$\wp E_{\mathrm{b}}[\mathbf{X}(\cdot,\cdot,\cdot,t)] = -\int_{\Omega} \frac{\partial^2}{\partial s^2} \left(c_{\mathrm{b}}(q, r, s) \left(\frac{\partial^2 \mathbf{X}^0}{\partial s^2} - \frac{\partial^2 \mathbf{X}}{\partial s^2} \right) \right) \cdot \wp \mathbf{X} \, \mathrm{d}q \, \mathrm{d}r \, \mathrm{d}s, \tag{3.70}$$

i.e., the bending-resistant force $\mathbf{F}_{\mathrm{b}}$ is

$$\mathbf{F}_{\mathrm{b}} = \frac{\partial^2}{\partial s^2} \left(c_{\mathrm{b}}(q, r, s) \left(\frac{\partial^2 \mathbf{X}^0}{\partial s^2} - \frac{\partial^2 \mathbf{X}}{\partial s^2} \right) \right). \tag{3.71}$$

Thus, the total Lagrangian force density corresponding to the forces generated by a system of elastic fibers which resist extension, compression, and bending is

$$\mathbf{F} = \mathbf{F}_{\mathrm{s}} + \mathbf{F}_{\mathrm{b}} = \frac{\partial}{\partial s} \left(T \boldsymbol{\tau} \right) + \frac{\partial^2}{\partial s^2} \left(c_{\mathrm{b}}(q, r, s) \left(\frac{\partial^2 \mathbf{X}^0}{\partial s^2} - \frac{\partial^2 \mathbf{X}}{\partial s^2} \right) \right). \tag{3.72}$$

In our simulations, we employ a simple finite difference discretization of **F** on the curvilinear mesh.

It is also possible to treat bending-resistant materials via a generalization of the immersed boundary method in which the immersed structure spreads both force and torque to the fluid, and in which the immersed structure moves according to both the interpolated linear velocity and the interpolated angular velocity of the fluid. Note, however, that this is *not* what is done in the present scheme. For further details, see Lim *et al.* [2008], which treats the particular case of an elastic beam immersed in a viscous incompressible fluid.

4. Simulating the Fluid Dynamics of Heart Valves

4.1. *The mitral heart valve*

We first apply the uniform grid version of the immersed boundary methodology described in the present work to the simulation of a model of a prosthetic mitral valve. The *native* mitral valve consists of two large leaflets, the anterior and posterior leaflets, along with smaller commissural leaflets, and is positioned between the left atrium and left ventricle of the heart. Fibrous chordae tendineae connect the free edges of the native mitral valve leaflets to papillary muscles in the left ventricle. When the heart contracts during systole, the papillary muscles pull on the chordae tendineae to prevent the mitral valve from bulging backwards into the left atrium, i.e., to prevent mitral prolapse. The prosthetic mitral valve which we simulate in the present study was developed by D. Wheatley's group in the Department of Cardiac Surgery at the University of Glasgow [Wheatley, 2002] and is designed to emulate the geometry and material properties of the native human mitral valve, including the chordae tendineae. The leaflets of the prosthetic valve are constructed out of a polyurethane material, and artificial chordae are embedded in the leaflets. Each of the chordae originates at the valve annulus, traverses either the anterior or posterior leaflet, and exits that leaflet via the free edge of the leaflet. The artificial chordae are intended to be attached to the papillary muscles in the left ventricle of the patient. The prosthetic valve includes 14 chordae in total, eight which are embedded in the posterior leaflet and six in the anterior leaflet. Although the native mitral valve displays a significant degree of anisotropy, the polyurethane material which is used to construct the prosthetic valve leaflets is isotropic. Nonetheless, the prosthetic valve leaflets are anisotropic because of the artificial chordae tendineae embedded in the leaflets.

The geometry and material properties of our model prosthetic mitral valve largely correspond to those of the actual prosthetic valve. A geometric description of the prosthetic valve is first generated using the SolidWorks CAD software, and the resulting CAD model is converted into a mesh which is decomposed into a network of one-dimensional elastic fibers. As described in Sec. 3, the elastic properties of the model valve (including the valve leaflets and the artificial chordae tendineae)

are represented in terms of a system of elastic fibers, and the material properties of these fibers are determined from the material properties of the prosthetic valve. Each leaflet has a mean thickness of 0.125 mm and is modelled as a linear material with a Young's modulus of 5.4 MPa, corresponding to the material properties of the actual prosthetic valve, although bending and shear stiffnesses are neglected in the model valve leaflets. The chordae are represented as one-dimensional fibers, and the material stiffnesses of these fibers are determined by considering each fiber to have a cross-sectional area of 0.4 mm^2 and a Young's modulus of 30 MPa, although the Young's modulus of the actual artificial chordae is 300 MPa. The smaller Young's modulus used in the model chordae is chosen to avoid the need to take excessively small timesteps. (Since our present timestepping scheme is only semi-implicit, stability considerations require that the size of the timestep be reduced as the stiffness of the material is increased.) The reference configurations for the stretching- and bending-resistant chordae are taken to be straight lines. See Watton *et al.* [2007, 2008] for additional details regarding the generation of the mitral valve model. The prosthetic mitral valve and the corresponding immersed boundary model are shown in Fig. 3.

For our immersed boundary simulation, the model mitral valve is mounted in a flow chamber, namely a semi-rigid circular pipe, which also is an immersed boundary model. The model valve and flow chamber are immersed in a rectangular 16 cm $\times$ 8 cm $\times$ 8 cm fluid region; see Fig. 4. Like the model valve, the model flow chamber is constructed out of fibers. In this case, the fibers resist extension, compression, and bending, and the no-stress reference configuration is taken to be the initial configuration. Additionally, target points are used to anchor the flow chamber in place. Unlike the simulations of Watton *et al.* [2008], in which a periodic velocity profile was used, here flow is driven through the model valve by prescribing physical boundary conditions at the upstream ($x = 0$ cm) and downstream ($x = 16$ cm) ends of the flow chamber. In particular, we prescribe a time-dependent parabolic velocity profile at the upstream boundary of the pipe and zero-pressure boundary conditions at the downstream end of the pipe. The time-dependent inflow velocity profile is chosen to yield flow rates which match those obtained from an experimental test rig [Watton *et al.*, 2008]. The measured inflow rates used in the mitral valve simulation are shown in Fig. 5. Solid wall boundary conditions are prescribed along the portions of the $x = 0$ cm and $x = 16$ cm boundaries which are *exterior* to the model flow chamber, and zero-pressure boundary conditions are employed along the remainder of the domain boundary.

The 14 chordae are anchored to two chordae attachment points (CAPs) which are located downstream of the model valve. Each CAP receives half of the chordae from each leaflet. The motion of the two CAPs is intended to mimic the motion of the papillary muscles in a real heart and is specified in the same manner as Watton *et al.* [2008]. For simplicity, the CAP motion is constrained to be in the streamwise direction only. The streamwise CAP displacements are shown in Fig. 5.

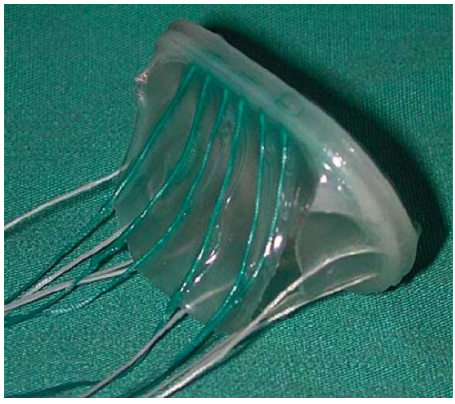

(A)

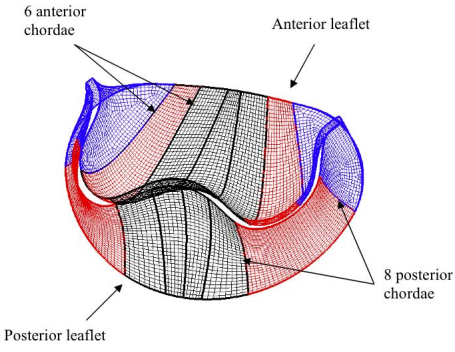

(B)

Fig. 3. (A) The chorded prosthetic mitral valve developed by D. Wheatley's group in the Department of Cardiac Surgery at University of Glasgow [Wheatley, 2002]. (B) The corresponding model prosthetic valve used in the present work. Although the chordae extend beyond the free edges of the model valve leaflets, only the portions of the chordae on the leaflets are shown in this panel.

The simulation is divided into two phases, a brief initialization phase followed by one flow cycle. The 15 ms initialization phase allows the valve to reach an approximate steady-state configuration. (Note that the reference configurations of the chordae are straight lines, and thus the valve is initialized in a stressed configuration.) During the initialization phase, no-flow boundary conditions are imposed at the upstream end of the pipe and zero-pressure boundary conditions are imposed at the downstream end of the pipe. The initialization phase is immediately followed by the 0.75 s flow cycle, during which flow is driven according to a prescribed upstream velocity profile. To facilitate comparisons with earlier simulations which use the same model [Watton *et al.*, 2007, 2008], we consider time $t = 0$ s to correspond to the beginning of the flow cycle, i.e., $t^0 = -15$ ms. Simulation results are shown in Figs. 6–9. In the present simulation, the peak pressure upstream of

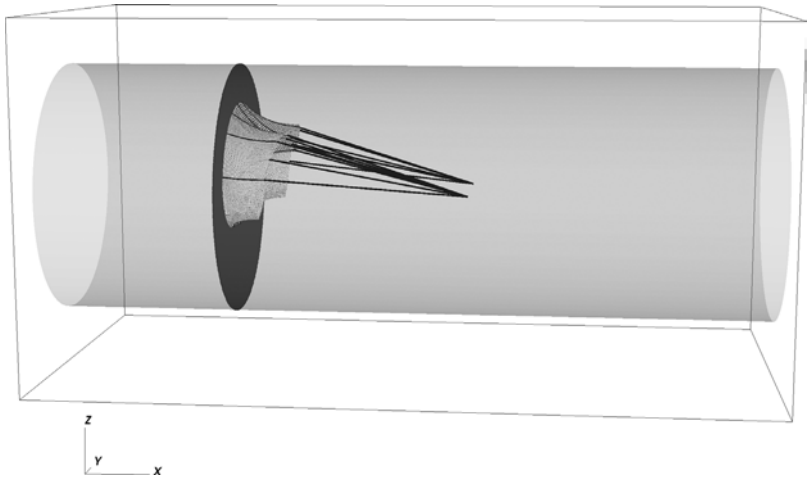

Fig. 4. The model mitral valve, mounted in a circular pipe and immersed in a rectangular fluid region. At the upstream end of the pipe, which is located at the left of the figure, a time-dependent parabolic velocity profile is prescribed in a manner that ensures that the inflow rate matches experimental measurements; see Fig. 5. At the downstream end of the pipe, which is located at the right of the figure, zero-pressure outflow boundary conditions are prescribed. The model chordae are anchored to two chordae attachment points (CAPs) which are located downstream of the model valve, and the motion of these two points is also specified; see Fig. 5. Each CAP receives half of the chordae from each leaflet. The distribution of the chordae between the two valve leaflets is shown in Fig. 3(B).

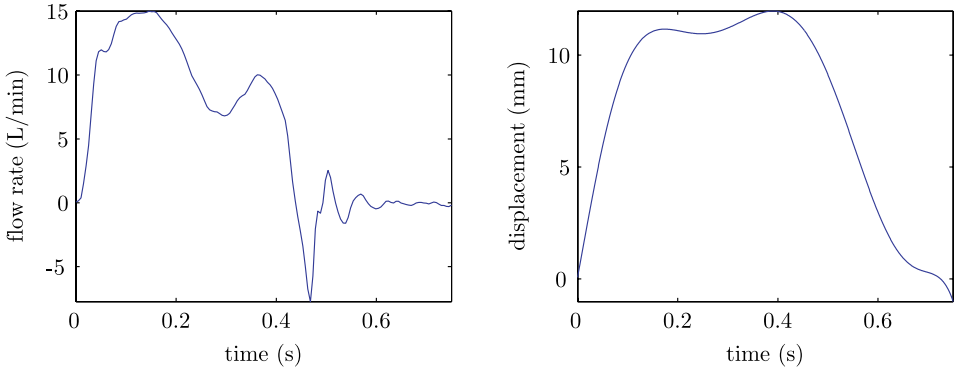

Fig. 5. (A) The experimentally measured inflow rate used to drive the mitral valve simulation. In the flow experiment in which these data were acquired, the flow was driven by a computer-controlled pump which generated pulsatile inflow. The flow volume was 80 ml per cycle, the cycle duration was 0.75 s (i.e., 80 cycles per minute), and the mean downstream pressure was 95 mmHg. (B) The streamwise displacement of the two CAPs as a function of time. The displacements used in the simulations are specified by a polynomial function which has been fit to physiological data (see Watton *et al.* [2008] for further details).

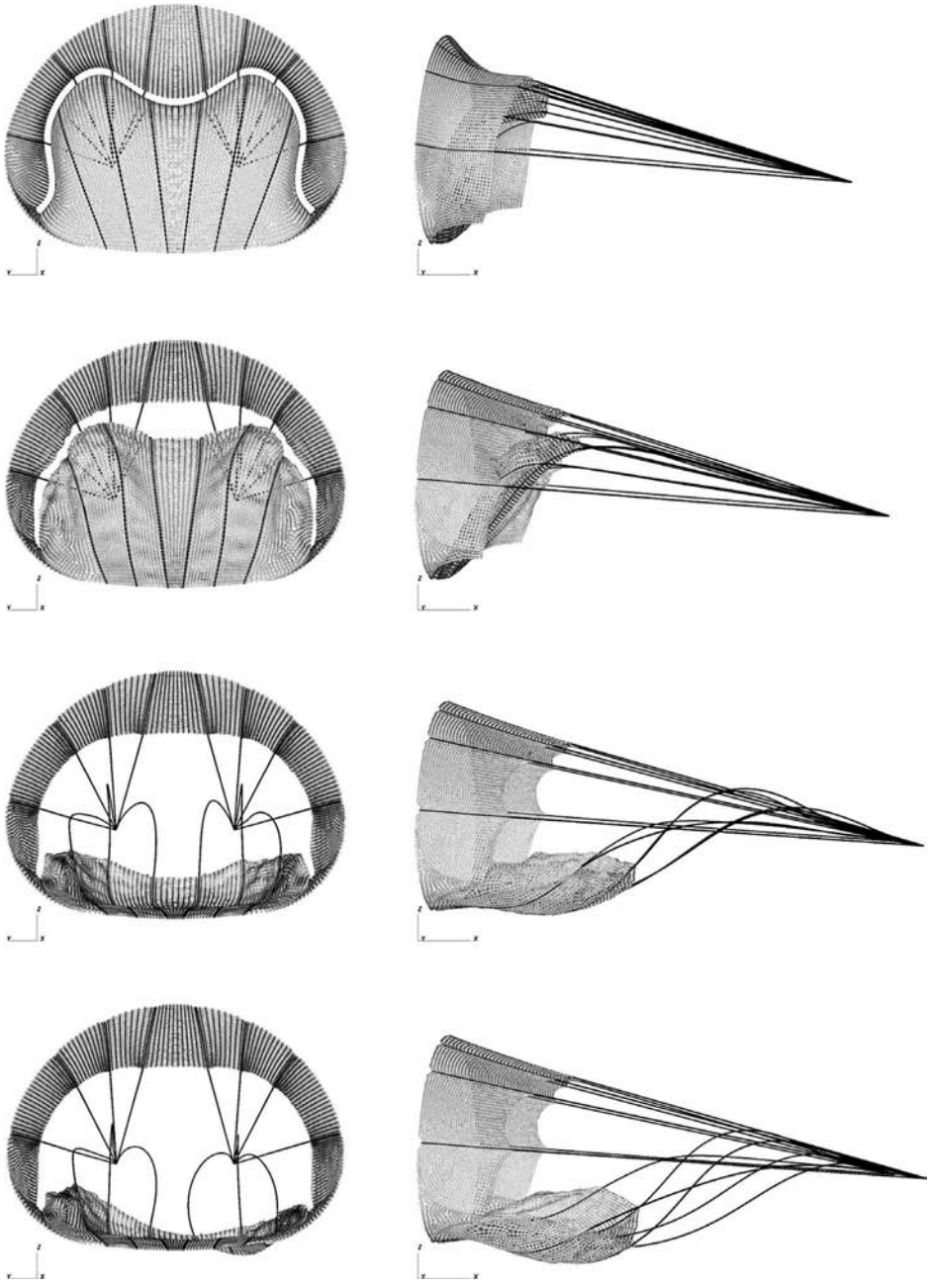

Fig. 6. The model mitral valve, including chordae, at different stages of opening, with the initial configuration of the valve shown in the top row. The valve is shown at equally spaced time intervals for $t = -0.015$ s to $t = 0.21$ s. In the left column, the valve is shown as viewed from the inflow boundary, so that the valve annulus is in the foreground, and the CAPs are in the background. The corresponding side view is shown in the right column. Note that the anterior leaflet is located near the bottom of each panel, and the posterior leaflet is located near the top.

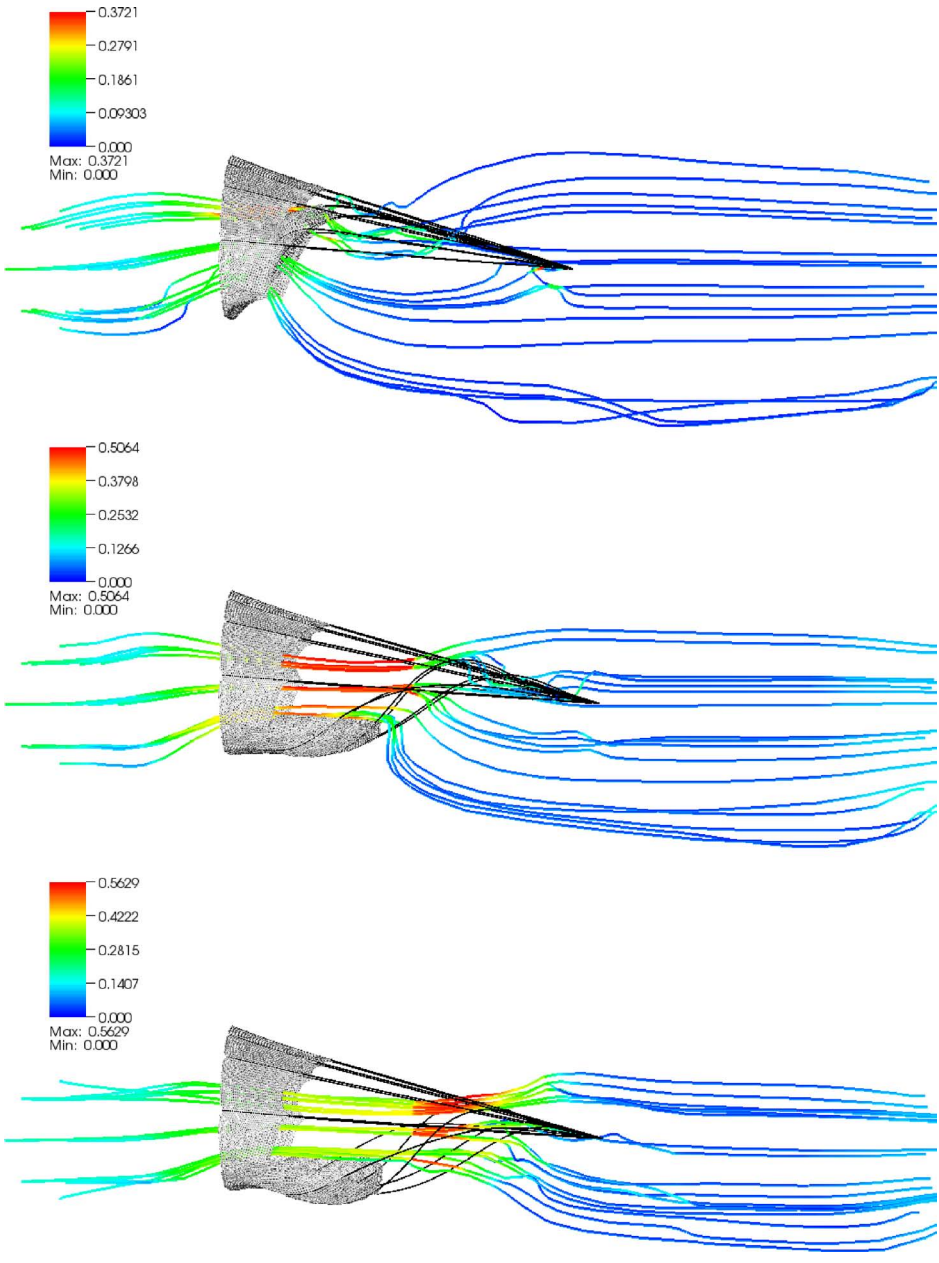

Fig. 7. Similar to Fig. 6, but here also showing instantaneous flow streamlines. The three panels of the present figure correspond to the bottom three rows of Fig. 6. (Note that the top row of Fig. 6 shows the initial configuration, for which there is no flow.) The streamlines are colored according to flow velocity with units of m/s. Note that in the top panel of this figure, the valve is just starting to open, and streamlines are seen to pass through the anterior valve leaflet. Such flow patterns are characteristic of moving boundary problems and, in particular, do not indicate that *fluid* is passing through the valve leaflet. Rather, in this case, the leaflet is essentially being carried with the flow.

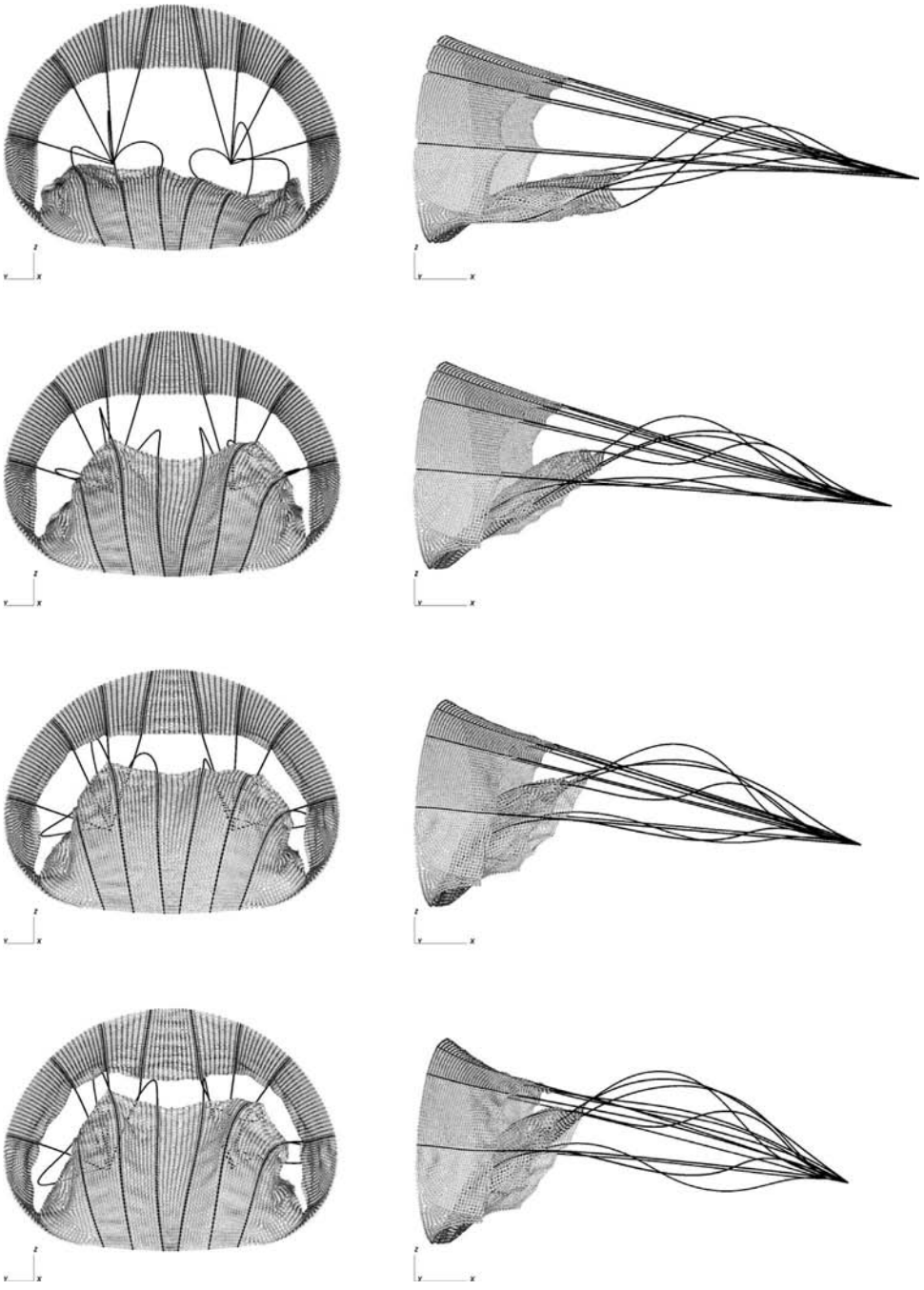

Fig. 8. Similar to Fig. 6, but here showing valve closure at equally spaced time intervals for $t = 0.48$ s to $t = 0.71$ s. We expect that the valve would close earlier and more completely if it were subjected to a significant systolic pressure load, but this has not yet been demonstrated.

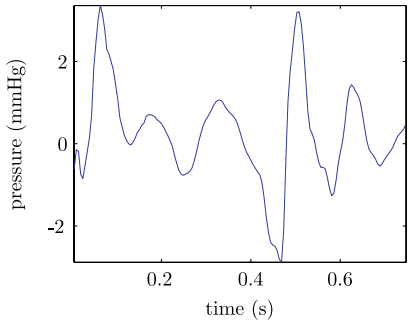

Fig. 9. The pressure 0.5 cm upstream of the model valve in reference to the 0 mmHg outlet pressure. Note that the peak pressure value attained during the simulation is 3.4 mmHg, which occurs at time $t = 0.063$ s. The time of the peak pressure can be used as an indicator of the time at which the valve opens. In our simulation, the model mitral valve opens at essentially the same time as it opens in the earlier simulations of Watton *et al.* [2007, 2008]; however, in the present simulation, a lower pressure is required to initiate valve opening in comparison to the pressure required in the earlier simulations.

the valve occurs at approximately time $t = 0.063$ s. The time of the peak pressure indicates the time at which the valve opens, and is in good agreement with earlier simulations using essentially the same valve model [Watton *et al.*, 2007, 2008]; however, the peak pressure in the present simulation is significantly reduced in comparison to the peak pressures of these earlier simulations. In particular, in the present simulation, the peak pressure upstream of the valve is approximately 3 mmHg; see See Fig. 9. In the earlier simulations, the peak pressure was approximately 12 mmHg. We attribute this difference largely to differences in the fluid solver. In the present simulation, the model valve also essentially closes near the end of the cycle, at approximately time $t = 0.7$ s; however, note that the model valve is not subjected to a significant pressure load during the systolic phase of the cardiac cycle. We expect that if the valve were subjected to a physiological pressure load, it would close earlier and more completely. The inclusion of more physiological loading conditions is left as future work.

4.2. *The aortic heart valve*

Using the methods described in this paper, we have also performed a spatially adaptive simulation of the fluid dynamics of a model of a natural aortic valve which is mounted in an idealized, semi-rigid model human aortic root. Our primary goal here is to demonstrate that it is feasible to perform three-dimensional immersed boundary simulations of the aortic valve in which realistic cardiac output is obtained at realistic blood pressures and with essentially no pressure drop across the open valve. Earlier three-dimensional immersed boundary simulations of cardiac fluid dynamics [Peskin and McQueen, 1996; McQueen and Peskin, 1997, 2000, 2001; Griffith *et al.*, 2007, 2009] all yielded either unphysiologically low flow rates at normal blood pressures, or normal flow rates at unphysiologically high pressures,

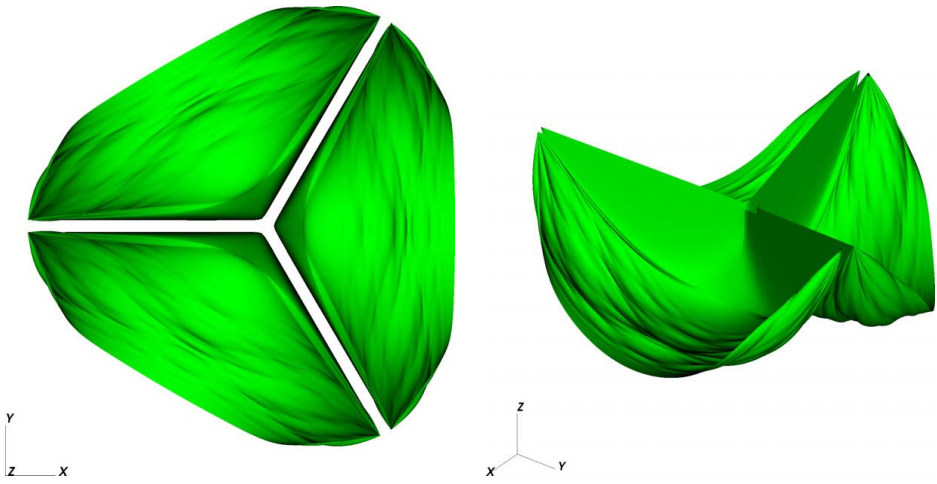

(A) (B)

Fig. 10. The initial configuration of the model aortic valve as viewed from above (A) and from the side (B).

but not normal flow rates at normal pressures. In the present work, we obtain significantly more realistic results by a combination of improved spatial resolution and improved numerical methods, although we suspect that further improvements in spatial resolution will prove necessary to obtain numerically converged results.

We model each of the aortic valve leaflets as a thin elastic membrane which is spanned by two continuous families of elastic fibers. One family of fibers runs from commissure to commissure and is constructed according to the mathematical theory of the fiber architecture of aortic heart valve leaflets described by Peskin and McQueen [1994]. The other family of fibers is comprised of fibers which are orthogonal to the commissural fibers. This second family of fibers is taken to be 20% as stiff as the commissural fibers. This crudely approximates the anisotropic material properties of real aortic valve leaflets, which are 10% as stiff in the radial direction as compared to the circumferential direction [Sauren, 1981]. The values of the commissural fiber stiffnesses employed in the model valve leaflets are chosen to be essentially the same as those used in earlier immersed boundary simulations of the fluid dynamics of the heart and its valves [Peskin and McQueen, 1996; McQueen and Peskin, 1997, 2000, 2001; Griffith *et al.*, 2007, 2009]. In these earlier simulations, the material properties of the aortic valve were empirically determined to yield a functioning valve. The shape of the model aortic root is based on the idealized geometric description of Reul *et al.* [1990], which was derived from angiographic films from 206 healthy patients, and the dimensions of the model vessel are based on measurements of human aortic roots harvested after autopsy which had been pressurized to a normal systolic pressure of 120 mmHg [Swanson and Clark, 1974]. The aortic wall is relatively thick (0.1 cm) [Shunk *et al.*, 2001] and

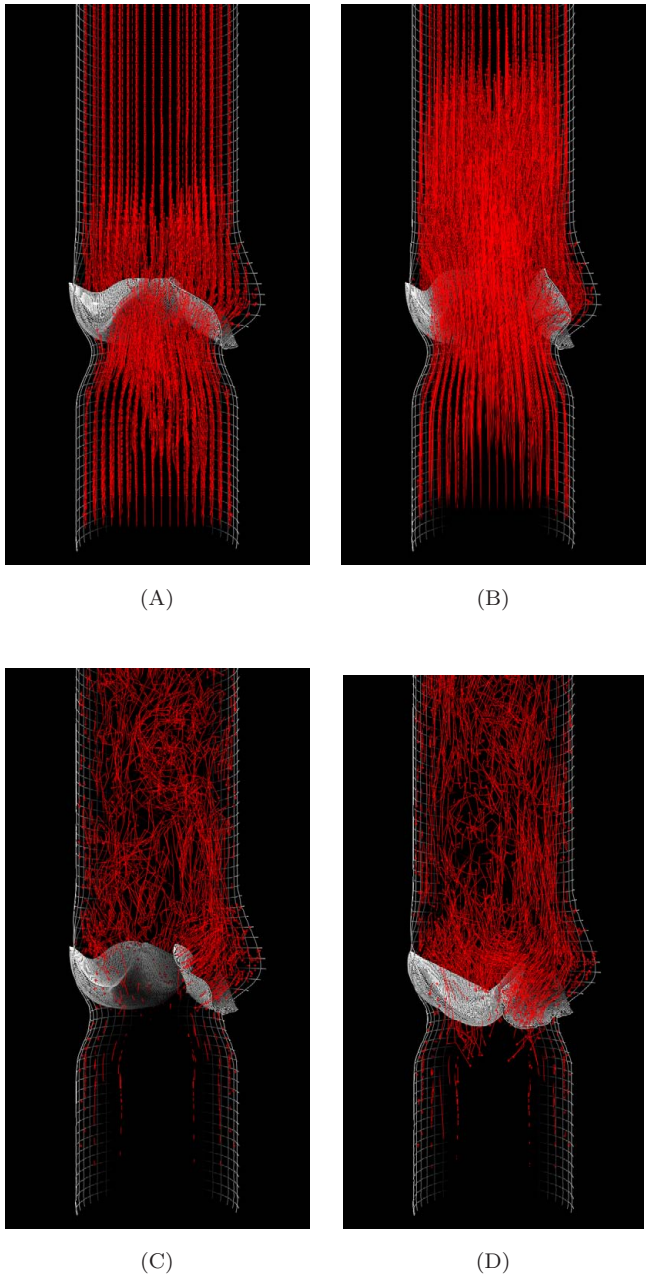

Fig. 11. The model valve and vessel along with passively advected red markers which indicate the motion of the blood within the model. In this view, the upstream ($z = 0$ cm) end of the model is located at the bottom of each panel, and the downstream ($z = 15$ cm) end of the model is located above the top of each panel. The model is shown just before (A) and after (B) valve opening (at approximately time $t = 0.15$ s), and just before (C) and after (D) valve closure (at approximately time $t = 0.4$ s). The open valve offers low flow resistance, allowing the model to generate physiological cardiac output. At the end of the cycle, the valve closes and allows only minor regurgitation.

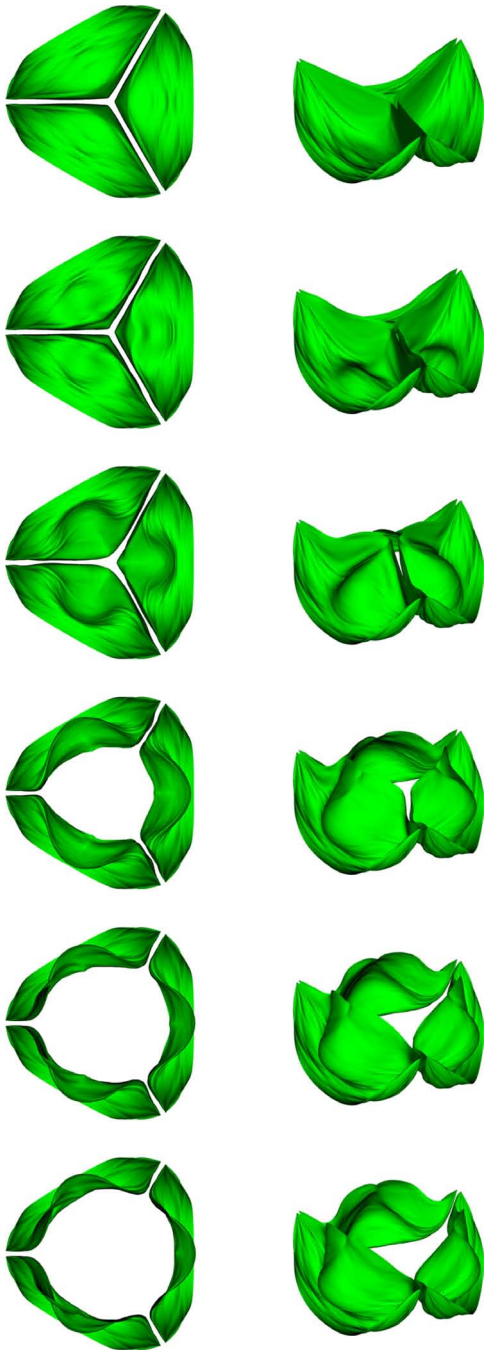

Fig. 12. The model aortic valve leaflets as the valve opens, shown at equally spaced time intervals from $t = 0.125$ s to $t = 0.189$ s. In the left column, the valve is shown as viewed from the downstream boundary. The corresponding side view is shown in the right column.

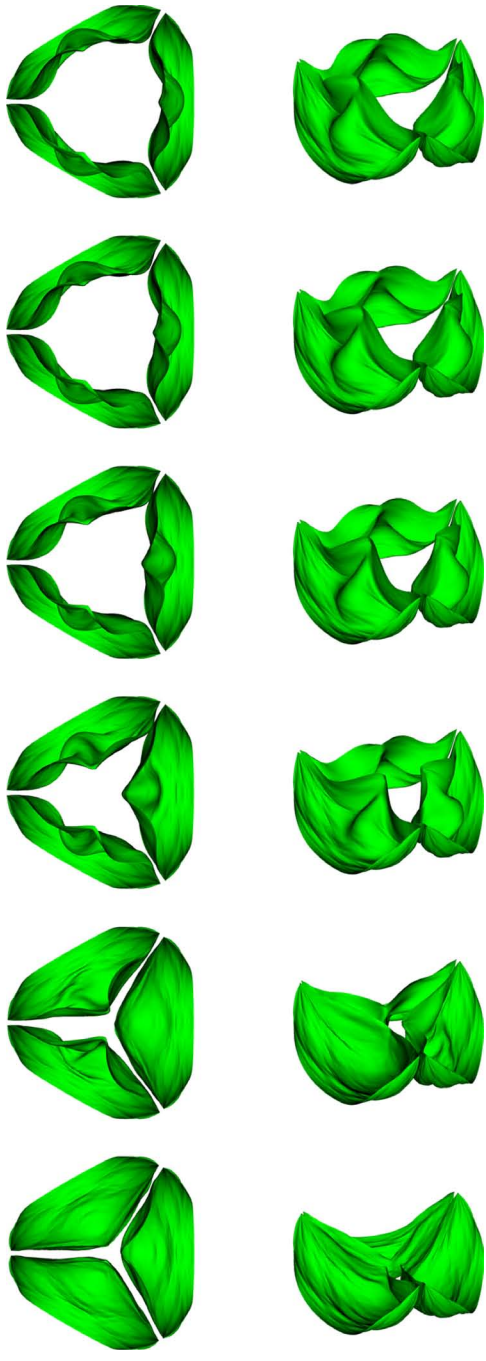

Fig. 13. Similar to Fig. 12, but here showing the model aortic valve leaflets as the valve closes at equally spaced time intervals from $t = 0.358$ s to $t = 0.406$ s. Note that when the valve closes, it nearly returns to the initial configuration shown in Fig. 10.

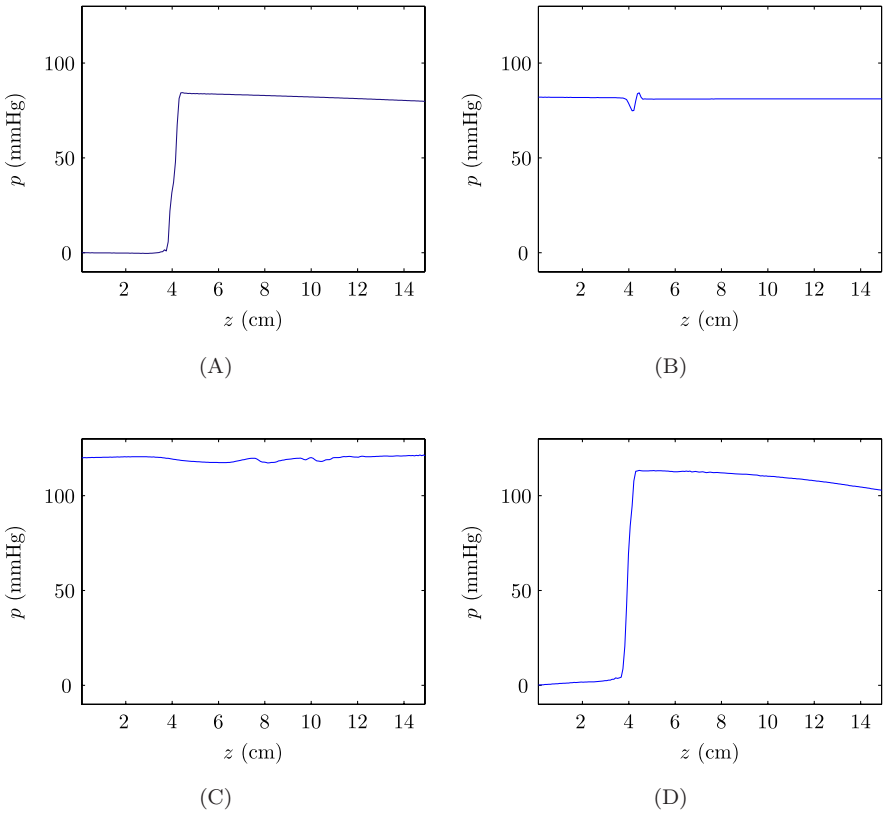

Fig. 14. Pressure as a function of distance along the center-line $(x, y) = (5\text{ cm}, 5\text{ cm})$ of the aortic valve model. The upstream end ($z = 0$ cm) of the model is connected to a specified, time-dependent pressure source which serves as a simplified model of the left ventricle. Following an initial pressurization phase, the downstream end ($z = 15$ cm) of the model is connected to a Windkessel model which serves as a reduced model of the systemic arterial tree. Pressure boundary conditions determined by these reduced models are prescribed both at the upstream and downstream boundaries. The valve itself is positioned at approximately $z = 4$ cm. (A) At the beginning of the simulation, we pressurize the downstream end of the domain to 85 mmHg, ensuring that the valve is closed and supports a significant, physiological pressure load. In this panel, the pressure is shown at time $t = 0.05$ s. (B) After the initial loading of the closed valve, we increase the pressure at the upstream boundary from 0 mmHg to 120 mmHg. In this panel, $t = 0.12$ s. At this time, the upstream and downstream pressures are approximately equal, and the valve is about to open. (C) After the valve opens, it offers very little flow resistance. Blood is accelerated as it passes through the open valve, causing a drop in pressure slightly downstream from the valve, followed by pressure recovery near the downstream boundary. The pressure is shown in this panel at time $t = 0.35$ s. (D) At the end of the cycle, the upstream pressure is returned to 0 mmHg. In this panel, $t = 0.45$ s. At this time, the valve has closed and is once again supporting a significant pressure load.

we model it as a "thick" structure (see Griffith and Peskin [2005]; Griffith *et al.* [2007]). Like the aortic valve leaflets, the aortic wall is constructed out of fibers; however, in this case, the material properties are taken to be isotropic. The material stiffnesses of these fibers are chosen so that the model vessel remains essentially

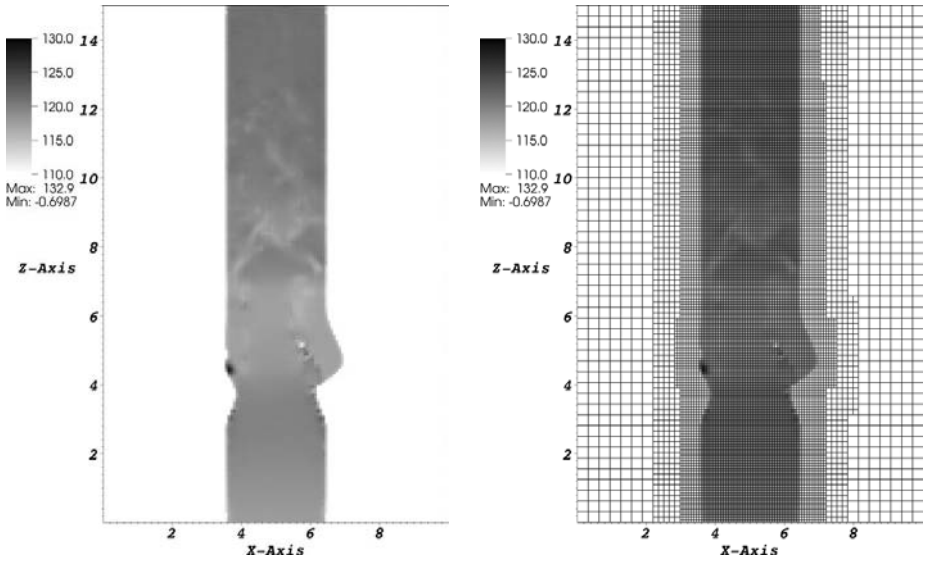

Fig. 15. (A) Hydrostatic pressure in the model aortic root plotted on the plane $y = 5$ cm, which bisects one of the valve leaflets. Note that these plotted values correspond to those of Fig. 14(C). See the caption of Fig. 14 for further details. (B) Same as (A), but with the adaptive grid also shown. Note that there are three levels of refinement and that the finest level covers the entire structure.

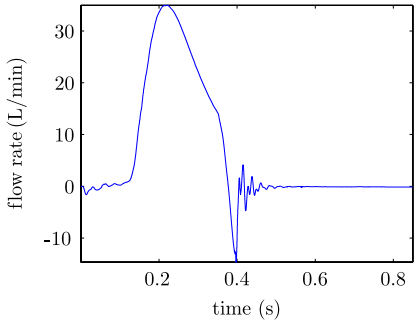

Fig. 16. Flow rate through the model aortic valve as a function of time. The stroke volume for this simulation is approximately 90 ml, which is within the physiological range. Although the valve allows minor regurgitation during closure, note that during the second half of the cycle, when the valve is fully closed, the valve allows no backflow.

stationary throughout the simulation. The valve leaflets are constructed using fibers which resist extension, compression, and bending, whereas the fibers which comprise the model vessel resist only extension and compression. Target points anchor the model vessel in place, allowing it to retain its shape despite its lack of bending rigidity. The no-stress reference configurations of the model valve leaflets are taken

to be the initial configuration of the leaflets, i.e., when deformed, the stretching- and bending-resistant forces attempt to return the valve leaflets to their initial configurations.[e]

For this simulation, the fluid domain is a rectangular 10 cm $\times$ 10 cm $\times$ 15 cm box. The upstream (ventricular) end of the aortic root model attaches to the $z = 0$ cm boundary of the fluid domain, and the downstream (aortic) end of the aortic root model attaches to the $z = 15$ cm boundary of the fluid domain. Pressure boundary conditions are provided at both the upstream and downstream ends of the model vessel. At the upstream boundary, a prescribed, time-dependent pressure source serves as a reduced model of the left ventricle. At the downstream boundary, the pressure is prescribed only during an initial pressurization phase. After this initial pressurization is complete, the downstream pressure is determined via a Windkessel model which has been fit to human data [Stergiopulos *et al.*, 1999] (note that we use the three-element Windkessel model of Stergiopulos *et al.* [1999], *not* the four-element Windkessel model described in that same paper). This ordinary differential equation model serves as a reduced model of the systemic arterial tree and provides realistic time-dependent loading for the model valve and vessel. Solid wall boundary conditions are prescribed along the portions of the $z = 0$ cm and $z = 15$ cm boundaries which are *exterior* to the model vessel, and zero-pressure boundary conditions are prescribed along the remaining exterior domain boundaries. A two-dimensional schematic diagram of the complete model, including both the prescribed upstream pressure source and the downstream reduced arterial tree model, is shown in Fig. 1.

The simulation consists of an initial pressurization phase which is followed by a single cardiac cycle. During the initial pressurization phase, the pressure at the downstream end of the model vessel is raised from 0 mmHg to 85 mmHg over the course of 0.05 s, and during this time, a small volume of fluid enters the vessel via the downstream boundary. After the initialization phase completes at $t = 0.05$ s, the pressure at that boundary is subsequently determined via the Windkessel model described above. At $t = 0.05$ s, we also begin the simulation of the cardiac cycle, starting with the onset of systolic contraction. During this phase of the simulation, we first raise the upstream pressure from 0 mmHg (corresponding to the end of diastole, when the heart is relaxed) to 120 mmHg (corresponding to peak systole, when the heart is fully contracted), doing so over the course of 0.1 s. We allow the

[e]Although the geometry of the model valve and vessel used in the present work is realistic, the material properties of the valve leaflets and vessel wall are not based on experimental data, but instead are empirically determined to yield a functioning model. The construction of immersed boundary models of the aortic valve and root which reproduce the material properties of real aortic valves and sinuses [Mirnajafi *et al.*, 2006; Stella *et al.*, 2007; Stella and Sacks, 2007; Gundiah *et al.*, 2008] remains future work. We are particularly interested in improving our description of the elasticity of the aortic root because real aortic sinuses are highly compliant, and the volume of the aortic root increases by approximately 35% during ejection [Lansac *et al.*, 2002]. In planned future studies, we aim to use a more realistic description of the material properties of the aortic sinuses and ascending aorta to study the role of the compliance of the aortic root in the fluid dynamics of the aortic valve in general, and in the formation of aortic sinus vortices in particular.

upstream pressure to remain at 120 mmHg for 0.2 s, and then, over the course of 0.1 s, reduce the upstream pressure to its resting diastolic value of 0 mmHg. The upstream pressure remains at 0 mmHg for the rest of the cardiac cycle. In total, we simulate 0.85 s, which includes the initial pressurization phase along with one complete cardiac cycle. In future work, we plan to replace these simple upstream driving pressures with realistic pressure waveforms [Murgo *et al.*, 1980].

Simulation results are presented in Figs. 11–16. During the course of the simulation, the maximum stretch ratio (i.e., the current length of a fiber segment divided by the resting length of that fiber segment) in the family of fibers running from commissure to commissure is approximately 1.10, and the minimum stretch ratio in that family of fibers is approximately 0.85. These fibers are maximally stretched near the centers of the leaflets (away from both the commissures and the vessel wall) during diastole, when the leaflets are bearing a physiological pressure load. The maximum and minimum stretch ratios for the second family of fibers (i.e., the family of fibers which is orthogonal to the commissural fibers) are approximately 1.65 and 0.35, respectively. For this family of fibers, maximum extension and compression both occur in small, concentrated regions near the commissural points during diastole. Further away from the commissural points (i.e., closer to the centers of the leaflets), the extension ratios in this second family of fibers are significantly closer to one.

Fig. 14 demonstrates that during forward flow, there is essentially no pressure drop across the open valve, i.e., this simulation appears to be sufficiently well resolved to avoid numerical stenosis. Additionally, although the valve allows a minor amount of regurgitation during closure, Figs. 14 and 16 demonstrate that once the valve closes fully, it allows no backflow while maintaining a significant, physiological pressure load. Stroke volume for this simulation is approximately 90 ml, which is within the physiological range [Guyton and Hall, 2000].

The present simulation of the aortic valve is similar to a series of three-dimensional simulations of the fluid dynamics of the aortic valve presented in de Hart [2002]; de Hart *et al.* [2003a,b, 2004]. The work of de Hart *et al.* employs a fictitious domain method which is not unlike the immersed boundary method, although in their work, a finite element description is employed both for the fluid and for the structure. Like the present model, the three-dimensional aortic valve and root model of de Hart *et al.* exhibits three-fold symmetry. Unlike the present simulation, however, the simulations of de Hart *et al.* exploit the symmetry of their model to reduce the cost of their computations. In particular, they employ symmetry boundary conditions which allow them simulate only one sixth of the aortic root (i.e., one half of one valve). Consequently, their model is unable to produce three-dimensional flow patterns which do not exhibit six-fold symmetry. We observe complex asymmetrical flow patterns in our simulation results, although it is not yet clear whether such patterns are the result of numerical under-resolution or are in fact physical flows.

A second key difference between the present model and the model of de Hart *et al.* is in the choice of physical boundary conditions. In the work of de Hart *et al.*,

time-dependent plug flow velocity boundary conditions are imposed at the upstream boundary of the aortic root, and a prescribed, time-dependent pressure waveform is imposed at the downstream boundary. Consequently, their model valve is not subjected to any significant pressure load during diastole, nor are the loading conditions able to respond to the actual flow through the valve. It seems likely that their simulation code could be adapted to impose pressure or stress boundary conditions at both ends of their model vessel, but it does not appear that this has been done. In the present work, pressure boundary conditions are prescribed at both the upstream and the downstream end of the model aortic root. Although the pressure source prescribed at the upstream boundary is somewhat simplistic, a realistic time-dependent pressure load is provided at the downstream boundary, and since the pressure load is determined by a Windkessel model, the loading conditions are able to adapt to the actual flow through the model valve and vessel. Moreover, in the present simulation, the model valve is not only subjected to a significant, physiological pressure load during the diastolic phase of the cardiac cycle; our model valve is shown to be able to support such a pressure load without leak.

4.3. *Heart sounds*

It has long been known that the familiar "lub-dup" heart sounds are caused by the closure of the heart valves, with the "lub" resulting from the closure of the mitral and tricuspid valves early in systole, and the "dup" resulting from the closure of the aortic and pulmonic valves at the end of systole. (Additional heart sounds in a patient can indicate various cardiovascular disorders.) In our simulation of the mitral valve, the "lub" sound may be seen in the prescribed inflow rate shown in Fig. 5. This is not surprising since this prescribed inflow rate was obtained from an actual flow experiment which used an actual prosthetic mitral valve. It is more significant that the "dup" heart sound generated by the closure of the aortic valve is clearly visible in the flow record presented in Fig. 16. This is notable because this flow record was not specified, but rather was *computed* as a part of the simulation. The "dup" heart sound may also be observed in the computed pressure waveforms, although these data are not shown.

5. Conclusions

In this paper, we have presented a version of the immersed boundary method which has been modified to allow the immersed elastic structures to approach closely to domain boundaries where physical boundary conditions are prescribed for the fluid, or to attach to such domain boundaries. Although we have considered only the specific case of a cell-centered Eulerian discretization and the four-point delta function, it is straightforward to adapt our extension of the immersed boundary method to alternative spatial discretizations and to different regularized delta functions. Indeed, we are presently completing the implementation of

a version of our modified immersed boundary scheme which uses a staggered-grid Eulerian spatial discretization. Unlike the cell-centered discretization of the present work, such schemes allow for the "exact" imposition of the discrete divergence-free condition with standard cell-centered Poisson solvers. Moreover, it is straightforward to develop unsplit time discretizations which may be used in conjunction with staggered-grid spatial discretizations [Griffith, submitted], thereby simplifying the treatment of physical boundary conditions on the fluid in comparison to projection methods [Brown *et al.*, 2001; Guy and Fogelson, 2005; Yang and Prosperetti, 2006]. The present modified immersed boundary scheme may also be used in conjunction with other standard immersed boundary delta functions. Some alternative regularized delta functions, such as the three-point delta function of Roma *et al.* [1999], may offer improved efficiency compared to the present four-point delta function, whereas other regularized delta functions, such as the six-point delta function of Stockie [1997], may yield improved accuracy compared to the standard four-point delta function for certain problems [Griffith and Peskin, 2005].

Our modified immersed boundary method allows us to connect detailed immersed boundary models to reduced (ordinary differential equation) models, such as Windkessel-type models of the systemic arterial tree, via physical boundary conditions. We expect that it would be straightforward to employ similar methods to connect a three-dimensional immersed boundary model to other kinds of reduced models, such as the one-dimensional network models of blood flow of Azer and Peskin [2007], but this has not yet been attempted. In earlier versions of the immersed boundary method, periodic boundary conditions were employed, and for such methods, it was necessary to use internal fluid sources and sinks to connect detailed immersed boundary models to reduced flow models [Griffith, 2005; Griffith *et al.*, 2007]. Of course, such internal sources and sinks may still be used with the present method; however, unlike earlier versions of the immersed boundary method, our version of the immersed boundary method is not *restricted* to using internal sources and sinks to provide driving and loading conditions.

The capabilities of our immersed boundary methodology have been demonstrated in the context of two different heart valve models, including a model of a chorded prosthetic mitral valve and a model of a natural aortic valve. In particular, we have demonstrated that it is feasible to perform three-dimensional immersed boundary simulations of heart valves in which realistic (physiological) flow rates are obtained at realistic fluid pressures. Presently, such simulations require significant computational resources; however, this is mainly a consequence of the severe stability restriction on the timestep size which is imposed by our present semi-implicit timestepping scheme. By building on recent work on implicit immersed boundary methods [Newren *et al.*, 2007, 2008; Mori and Peskin, 2008], we expect that it will be possible to reduce substantially the expense of these computations, thereby allowing more realistic and comprehensive simulations of cardiovascular fluid dynamics.

Acknowledgments

This work was sponsored in part by a grant from the American Heart Association to BEG. We are also grateful for funding provided by the British Heart Foundation, the Royal Society of Edinburgh, and the Royal Academy of Engineering. All simulations were performed at New York University using computer facilities funded in large part by a generous donation by St. Jude Medical, Inc.

References

Almgren, A. S., Bell, J. B., Colella, P., Howell, L. H. and Welcome, M. L. [1998] A conservative adaptive projection method for the variable density incompressible Navier-Stokes equations, *Journal of Computational Physics* **142**(1), 1–46.

Almgren, A. S., Bell, J. B. and Crutchfield, W. Y. [2000] Approximate projection methods: Part I. Inviscid analysis, *SIAM Journal on Scientific Computing* **22**(4), 1139–1159.

Almgren, A. S., Bell, J. B. and Szymczak, W. G. [1996] A numerical method for the incompressible Navier-Stokes equations based on an approximate projection, *SIAM Journal on Scientific Computing* **17**(2), 358–369.

Azer, K. and Peskin, C. S. [2007] A one-dimensional model of blood flow in arteries with friction and convection based on the Womersley velocity profile, *Cardiovascular Engineering* **7**(2), 51–73.

Bell, J. B., Colella, P. and Glaz, H. M. [1989] A second-order projection method for the incompressible Navier-Stokes equations, *Journal of Computational Physics* **85**(2), 257–283.

Bodony, D. J. [2006] Analysis of sponge zones for computational fluid mechanics, *Journal of Computational Physics* **212**(2), 681–702.

Brown, D. L., Cortez, R. and Minion, M. L. [2001] Accurate projection methods for the incompressible Navier-Stokes equations, *Journal of Computational Physics* **168**(2), 464–499.

Chorin, A. J. [1968] Numerical solution of the Navier-Stokes equations, *Mathematics of Computation* **22**(104), 745–762.

Chorin, A. J. [1969] On the convergence of discrete approximations to the Navier-Stokes equations, *Mathematics of Computation* **23**(106), 341–353.

Colella, P. and Woodward, P. R. [1984] The piecewise parabolic method (PPM) for gas-dynamical simulations, *Journal of Computational Physics* **54**(1), 174–201.

de Hart, J. [2002] *Fluid-Structure Interaction in the Aortic Heart Valve: A Three-Dimensional Computational Analysis*, PhD thesis, Technische Universiteit Eindhoven.

de Hart, J., Baaijens, F. P. T., Peters, G. W. M. and Schreurs, P. J. G. [2003a] A computational fluid-structure interaction analysis of a fiber-reinforced stentless aortic valve, *Journal of Biomechanics* **36**(5), 699–712.

de Hart, J., Peters, G. W. M., Schreurs, P. J. G. and Baaijens, F. P. T. [2004] Collagen fibers reduce stresses and stabilize motion of aortic valve leaflets during systole, *Journal of Biomechanics* **37**(3), 303–311.

de Hart, J., Peters, G. W. M., Schreurs, P. J. G. and Baaijens, F. P. T. [2003b] A three-dimensional computational analysis of fluid-structure interaction in the aortic valve, *Journal of Biomechanics* **36**(1), 102–112.

Gottlieb, S., Shu, C.-W. and Tadmor, E. [2001] Strong stability-preserving high-order time discretization methods, *SIAM Review* **43**(1), 89–112.

Gresho, P. M. and Sani, R. L. [1998] *Incompressible Flow and the Finite Element Method: Advection-Diffusion and Isothermal Laminar Flow* (John Wiley & Sons).

Griffith, B. E. [2005] *Simulating the Blood-Muscle-Valve Mechanics of the Heart by an Adaptive and Parallel Version of the Immersed Boundary Method*, PhD thesis, Courant Institute of Mathematical Sciences, New York University.

Griffith, B. E. [submitted] An accurate and efficient method for the incompressible Navier-Stokes equations using the projection method as a preconditioner, Submitted to *Journal of Computational Physics*.

Griffith, B. E., Hornung, R. D., McQueen, D. M. and Peskin, C. S. [2007] An adaptive, formally second order accurate version of the immersed boundary method, *Journal of Computational Physics* **223**(1), 10–49.

Griffith, B. E., Hornung, R. D., McQueen, D. M. and Peskin, C. S. [2009] Parallel and adaptive simulation of cardiac fluid dynamics, in M. Parashar, S. Chandra and X. Li (eds.), *Advanced Computational Infrastructures for Parallel and Distributed Adaptive Applications* (John Wiley and Sons), expected publication in May, 2009.

Griffith, B. E. and Peskin, C. S. [2005] On the order of accuracy of the immersed boundary method: Higher order convergence rates for sufficiently smooth problems, *Journal of Computational Physics* **208**(1), 75–105.

Gundiah, N., Kam, K., Matthews, P. B., Guccione, J., Dwyer, H. A., Saloner, D., Chuter, T. A. M., Guy, T. S., Ratcliffe, M. B. and Tseng, E. E. [2008] Asymmetric mechanical properties of porcine aortic sinuses, *Annals of Thoracic Surgery* **85**(5), 1631–1638.

Guy, R. D. and Fogelson, A. L. [2005] Stability of approximate projection methods on cell-centered grids, *Journal of Computational Physics* **203**(2), 517–538.

Guyton, A. C. and Hall, J. E. [2000] *Textbook of Medical Physiology, Tenth Edition* (W. B. Saunders Company, Philadelphia, PA, USA).

Kim, Y. [2003] *The Penalty Immersed Boundary Method and its Applications to Aerodynamics*, PhD thesis, Courant Institute of Mathematical Sciences, New York University.

Kim, Y. and Peskin, C. S. [2006] 2-D parachute simulation by the immersed boundary method, *SIAM Journal on Scientific Computing* **28**(6), 2294–2312.

Kim, Y. and Peskin, C. S. [2007] Penalty immersed boundary method for an elastic boundary with mass, *Physics of Fluids* **19**, 053103 (18 pages).

Kim, Y., Zhu, L., Wang, X. and Peskin, C. S. [2003] On various techniques for computer simulation of boundaries with mass, in K. J. Bathe (ed.), *Proceedings of the Second MIT Conference on Computational Fluid and Solid Mechanics* (Elsevier), pp. 1746–1750.

Lai, M. F. [1993] *A Projection Method for Reacting Flow in the Zero Mach Number Limit*, PhD thesis, University of California at Berkeley.

Lansac, E., Lim, H. S., Shomura, Y., Lim, K. H., Goetz, W., Rice, N. T., Acar, C. and Duran, C. M. G. [2002] Aortic and pulmonary root: are their dynamics similar? *European Journal of Cardio-thoracic Surgery* **21**(2), 268–275.

Lim, S., Ferent, A., Wang, X. S. and Peskin, C. S. [2008] Dynamics of a closed rod with twist and bend in fluid, *SIAM Journal on Scientific Computing* **31**(1), 273–302.

Martin, D. F. and Colella, P. [2000] A cell-centered adaptive projection method for the incompressible Euler equations, *Journal of Computational Physics* **163**(2), 271–312.

Martin, D. F., Colella, P. and Graves, D. [2008] A cell-centered adaptive projection method for the incompressible Navier-Stokes equations in three dimensions, *Journal of Computational Physics* **227**(3), 1863–1886.

McQueen, D. M. and Peskin, C. S. [1997] Shared-memory parallel vector implementation of the immersed boundary method for the computation of blood flow in the beating mammalian heart, *Journal of Supercomputing* **11**(3), 213–236.

McQueen, D. M. and Peskin, C. S. [2000] A three-dimensional computer model of the human heart for studying cardiac fluid dynamics, *Computer Graphics* **34**(1), 56–60.

McQueen, D. M. and Peskin, C. S. [2001] Heart simulation by an immersed boundary method with formal second-order accuracy and reduced numerical viscosity, in H. Aref and J. W. Phillips (eds.), *Mechanics for a New Millennium, Proceedings of the 20th International Conference on Theoretical and Applied Mechanics (ICTAM 2000)* (Kluwer Academic Publishers).

Mirnajafi, A., Raymer, J. M., McClure, L. R. and Sacks, M. S. [2006] The flexural rigidity of the aortic valve leaflet in the commissural region, *Journal of Biomechanics* **39**(16), 2966–2973.

Mori, Y. and Peskin, C. S. [2008] Implicit second order immersed boundary methods with boundary mass, *Computational Methods in Applied Mechanics and Engineering* **197**(25–28).

Murgo, J. P., Westerhof, N., Giolma, J. P. and Altobelli, S. A. [1980] Aortic input impedance in normal man: relationship to pressure wave forms, *Circulation* **62**(1), 105–116.

Newren, E. P., Fogelson, A. L., Guy, R. D. and Kirby, R. M. [2007] Unconditionally stable discretizations of the immersed boundary equations, *Journal of Computational Physics* **222**(2), 702–719.

Newren, E. P., Fogelson, A. L., Guy, R. D. and Kirby, R. M. [2008] A comparison of implicit solvers for the immersed boundary equations, *Computational Methods in Applied Mechanics and Engineering* **197**(25–28).

Peskin, C. S. [1972] *Flow patterns around heart valves: A digital computer method for solving the equations of motion*, PhD thesis, Albert Einstein College of Medicine.

Peskin, C. S. [1977] Numerical analysis of blood flow in the heart, *Journal of Computational Physics* **25**(3), 220–252.

Peskin, C. S. [2002] The immersed boundary method, *Acta Numerica* **11**, 479–517.

Peskin, C. S. and McQueen, D. M. [1994] Mechanical equilibrium determines the fractal fiber architecture of aortic heart valve leaflets, *American Journal of Physiology-Heart and Circulatory Physiology* **266**(1), H319–H328.

Peskin, C. S. and McQueen, D. M. [1996] Fluid dynamics of the heart and its valves, in H. G. Othmer, F. R. Adler, M. A. Lewis and J. C. Dallon (eds.), *Case Studies in Mathematical Modeling: Ecology, Physiology, and Cell Biology* (Prentice-Hall, Englewood Cliffs, NJ, USA), pp. 309–337.

Reul, H., Vahlbruch, A., Giersiepen, M., Schmitz-Rode, T., Hirtz, V. and Effert, S. [1990] The geometry of the aortic root in health, at valve disease and after valve replacement, *Journal of Biomechanics* **23**, 181–191.

Rider, W. J., Greenough, J. A. and Kamm, J. R. [2007] Accurate monotonicity- and extrema-preserving methods through adaptive nonlinear hybridizations, *Journal of Computational Physics* **225**(2), 1827–1848.

Roma, A. M., Peskin, C. S. and Berger, M. J. [1999] An adaptive version of the immersed boundary method, *Journal of Computational Physics* **153**(2), 509–534.

Sauren, A. A. H. J. [1981] *The Mechanical Behaviour of the Aortic Valve*, PhD thesis, Technische Universiteit Eindhoven.

Shunk, K. A., Garot, J., Atalar, E. and Lima, J. A. C. [2001] Transecophageal Magnetic Resonance Imaging of the aortic arch and descending thoracic aorta in patients with aortic atherosclerosis, *Journal of the American College of Cardiology* **37**(8), 2031–2035.

Stella, J. A., Liao, J. and Sacks, M. S. [2007] Time-dependent biaxial mechanical behavior of the aortic heart valve leaflet, *Journal of Biomechanics* **40**(14), 3169–3177.

Stella, J. A. and Sacks, M. S. [2007] On the biaxial mechanical properties of the layers of the aortic valve leaflet, *Journal of Biomechanical Engineering* **129**(5), 757–766.

Stergiopulos, N., Westerhof, B. E. and Westerhof, N. [1999] Total arterial inertance as the fourth element of the windkessel model, *American Journal of Physiology–Heart and Circulatory Physiology* **276**(1), H81–H88.

Stockie, J. M. [1997] *Analysis and computation of immersed boundaries, with application to pulp fibres*, PhD thesis, Institute of Applied Mathematics, University of British Columbia.

Swanson, M. and Clark, R. E. [1974] Dimensions and geometric relationships of the human aortic valve as a function of pressure, *Circulation Research* **35**(6), 871–882.

Watton, P. N., Luo, X. Y., Wang, X., Bernacca, G. M., Molloy, P. and Wheatley, D. J. [2007] Dynamic modelling of prosthetic chorded mitral valves using the immersed boundary method, *Journal of Biomechanics* **40**(3), 613–626.

Watton, P. N., Luo, X. Y., Yin, M., Bernacca, G. M. and Wheatley, D. J. [2008] Effect of ventricle motion on the dynamic behaviour of chorded mitral valves, *Journal of Fluids and Structures* **24**(1), 58–74.

Wheatley, D. J. [2002] Mitral valve prosthesis, Patent number WO03037227.

Yang, B. and Prosperetti, A. [2006] A second-order boundary-fitted projection method for free-surface flow computations, *Journal of Computational Physics* **213**(2), 574–590.

Zhu, L. and Peskin, C. S. [2002] Simulation of a flapping flexible filament in a flowing soap film by the immersed boundary method, *Journal of Computational Physics* **179**(2), 452–468.

Zhu, L. and Peskin, C. S. [2003] Interaction of two flapping filaments in a flowing soap film, *Physics of Fluids* **15**(7), 1954–1960.